Theory of the carbon vacancy in 4*H*-SiC: Crystal field and pseudo-Jahn-Teller effects

José Coutinho* and Vitor J. B. Torres
Department of Physics and I3N, University of Aveiro, Campus Santiago, 3810-193 Aveiro, Portugal

Kamel Demmouche
Institut des Sciences, Centre Universitaire -Belhadj Bouchaib- Ain Temouchent, Route de Sidi Bel Abbes, B.P. 284, 46000 Ain Temouchent, Algeria

Sven Öberg
Department of Engineering Sciences and Mathematics, Luleå University of Technology, SE-97187 Luleå, Sweden
(Received 30 August 2017; published 6 November 2017)

The carbon vacancy in 4*H*-SiC is a powerful minority carrier recombination center in as-grown material and a major cause of degradation of SiC-based devices. Despite the extensiveness and maturity of the literature regarding the characterization and modeling of the defect, many fundamental questions persist. Among them, we have the shaky connection of the EPR data to the electrical measurements lacking sublattice site resolution, the physical origin of the pseudo-Jahn-Teller effect, the reasoning for the observed sublattice dependence of the paramagnetic states, and the severe temperature dependence of some hyperfine signals, which cannot be accounted for by a thermally activated dynamic averaging between equivalent Jahn-Teller distorted structures. In this work, we address these problems by means of semilocal and hybrid density functional calculations. We start by inventorying a total of four different vacancy structures from the analysis of relative energies. Diamagnetic states have well defined low-energy structures, whereas paramagnetic states display metastability. The reasoning for the rich structural variety is traced back to the filling of electronic states which are shaped by a crystal-field-dependent (and therefore site-dependent) pseudo-Jahn-Teller effect. From calculated minimum energy paths for defect rotation and transformation mechanisms, combined with the calculated formation energies and electrical levels, we arrived at a configuration-coordinate diagram of the defect. The diagram provides us with a detailed first-principles picture of the defect when subject to thermal excitations. The calculated acceptor and donor transitions agree well with the binding energies of electrons emitted from the $Z_{1/2}$ and $EH_{6/7}$ traps, respectively. From the comparison of calculated and measured U-values, and correlating the site-dependent formation energies with the relative intensity of the DLTS peaks in as-grown material, we assign Z_1 (EH_6) and Z_2 (EH_7) signals to acceptor (donor) transitions of carbon vacancies located on the h and k sublattice sites, respectively.

DOI: 10.1103/PhysRevB.96.174105

I. INTRODUCTION

A wide and indirect band gap, high chemical and thermal stability, as well as radiation and electrical hardness, are among the merits that make silicon carbide (SiC) an outstanding material for high-voltage and high-power electronics [1,2]. Due to its superior properties, the 4*H*-SiC polytype has been the material of choice of the industry. However, the presence of carbon-related point defects in SiC, particularly carbon vacancies (V_C), is a major cause for minority carrier recombination in n-type material and device failures like low field effect mobility [3,4]. These problems have been connected to a set of V_C-related deep traps measured by deep-level transient spectroscopy (DLTS) and labelled $Z_{1/2}$ and $EH_{6/7}$ [5–7].

The $Z_{1/2}$ has been ascribed to the superposition of Z_1 and Z_2 signals, each of which arising from a $V_C(=/0)$ two-electron emission cascade at distinct sublattice sites of the 4*H* polytype [8–10]. Defects behaving like that are said to possess a negative-U as they show an *inverted order* of energy levels [11]. This is possible thanks to a strong atomic relaxation somewhere along the emission sequence. For the case of $Z_{1/2}$ this translates into the appearance of a $(=/0)$ occupancy level at about $E_c - 0.6$ eV, implying that the formation of negatively charged vacancies (V_C^-) is always energetically unfavorable against the formation of any mix of neutral (V_C^0) and double negative ($V_C^=$) defects, no matter the position of the Fermi energy. The appearance of V_C^- is most likely when the Fermi level lies at the $(=/0)$ transition energy, where its formation energy, E_f, is lowest with respect to other charge states. Depending on the temperature and the energy difference $2E_f(V_C^-) - E_f(V_C^= + V_C^0)$, some V_C^- states can still be populated. Alternatively, V_C^- can be formed from other charge states after capture/emission of carriers upon optical excitation. The actual $Z_1(=/-)$ and $Z_1(-/0)$ levels were, respectively, measured at 0.67 eV and ∼0.52 eV below E_c, whereas $Z_2(=/-)$ and $Z_2(-/0)$ were found at about $E_c - 0.71$ eV and $\sim E_c - 0.45$ eV, respectively [8–10]. Also noteworthy is the fact that in 6*H*-SiC, a pair of electron traps located at $\sim E_c - 0.4$ eV and labeled E_1/E_2 from DLTS measurements, were attributed to acceptor transitions from equivalent defects at different sublattice sites [12,13]. More recently, high-resolution Laplace-DLTS was able to further resolve E_1/E_2 into three components, and based on their similarity with $Z_{1/2}$ (including their capture cross section

*jose.coutinho@ua.pt

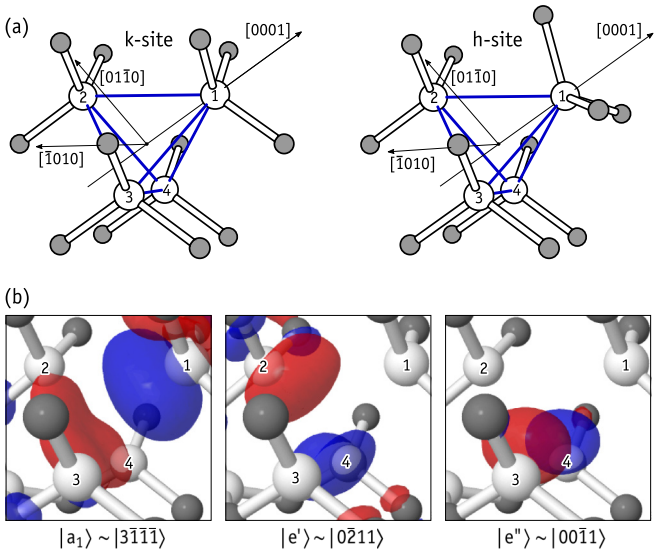

FIG. 1. (a) Atomic structure of perfect carbon vacancies at k and h sites of a 4H-SiC crystal. Si and C atoms are white and gray, respectively. Si_1 is axial (located on the [0001] crystallographic axis), whereas $Si_{2\text{-}4}$ atoms lie on the basal plane. (b) Representation of the one-electron states in the gap ($a_1 + e$) arising from an undistorted V_C defect at the k site. Red and blue isosurfaces denote negative and positive phases, respectively.

and negative-U ordering of levels), they were assigned to the carbon vacancy located on all three available sites (h, k_1, and k_2) of the 6H polytype [14].

The $EH_{6/7}$ DLTS band has been a subject of discussion and surrounded by some controversy. It usually shows up with a magnitude lower than $Z_{1/2}$ [15], and it is made of two nearly overlapping peaks, apparently with varying amplitude ratio (between 1:3 and 1:5) depending on sample conditions [16,17]. These facts led to suggestions that $EH_{6/7}$ should not have the same origin of $Z_{1/2}$, but rather be connected to a complex involving V_C [18–21]. Recently, Booker and co-workers [17] analyzed the $EH_{6/7}$ capacitance transients, and based on a three-charge state model they concluded that like $Z_{1/2}$, the $EH_{6/7}$ band results from two correlated, two-electron emission processes from two defects. Most importantly, they found that the concentration ratio of EH_6:EH_7 is 1:1 if we consider that the stronger peak actually combines $EH_7(0/+)$, $EH_7(+/++)$ and $EH_6(+/++)$ transitions, while the smaller component of the band comes from $EH_6(0/+)$ alone. The issue of the inconsistent magnitude ratio between $EH_{6/7}$ and $Z_{1/2}$ was poorly addressed. For all these transitions, carrier binding energies were measured at $E_c - 1.50$, $E_c - 1.46$, $E_c - 1.48$, and about $E_c - 1.42$–1.49 eV, respectively. This suggests that EH_7 is a negative-U defect, while that cannot be said for EH_6 due to uncertainty in the measurements.

Before continuing, let us introduce some notation with the help of Fig. 1(a). Here we depict the atomic structure of perfect V_C defects at k and h sites (with k and h labels referring to quasicubic and quasihexagonal sublattice sites of the 4H-SiC crystal). For the sake of convenience, the atom numbering scheme was chosen in line with previous works in the literature [22,23]. Hence, for a trigonal structure, we have Si_1 (axial) and $Si_{2\text{-}4}$ (basal) shells of Si atoms. For monoclinic structures we assume Si_1 and Si_2 to lie on the ($\bar{1}$010) mirror plane and the $Si_{3,4}$ pair to be mirror-symmetric. Hereafter, $V_C^q(s)$ refers to the carbon vacancy at the sublattice site $s \in \{k, h\}$ and charge state $q \in \{=, -, 0, +, ++\}$ (from double minus to double plus). Occasionally, we may also distinguish a vacancy with a specific atomic geometry R as $V_C^q(s, R)$. We also introduce at this point a way to represent the vacancy electronic states using simple linear combination of atomic orbitals (LCAO). Accordingly, a state $|\alpha_1\alpha_2\alpha_3\alpha_4\rangle$ stands for $A\sum_i \alpha_i\phi_i$, where A is a normalization constant, α_i are hybridization coefficients, and the summation runs over all four Si_i radical states ϕ_i (with $i = 1, \ldots, 4$).

Many details about the electronic and atomistic structure of V_C in 4H-SiC, particularly in their paramagnetic V_C^+ and V_C^- states, could be unraveled by electron paramagnetic resonance (EPR) measurements [10,24–30]. Among these reports, those combining experiments with first-principles calculations [23,28–30] turn out to be particularly elucidating. Below we provide a brief summary of those results, with a special focus on the relevant issues for the purpose of this work.

In p-type material irradiated with MeV electrons at high temperatures (850°C), the EPR spectrum revealed two signals, labeled as EI5 (also referred to as Ky1/Ky2/ID1) and EI6 (also Ky3/ID2), which were assigned to $V_C^+(k)$ and $V_C^+(h)$, respectively [23,25–28]. Below $T \approx 50$ K the main line of $V_C^+(k)$ exhibited C_{1h} symmetry, and was accompanied by three distinct hyperfine (HF) signals due to interactions between the electron spin and ^{29}Si nuclei in shells with 1, 1, and 2 atoms. Above 50 K the spectrum was converted to a trigonal (C_{3v}) pattern with two HFs representative of one axial Si atom and three equivalent Si atoms on the basal plane. From the temperature dependence of the HF lifetimes, the conversion from monoclinic to trigonal symmetry was estimated to be limited by a barrier as low as 0.014 eV [23]. $V_C^+(h)$ on the other hand, always showed trigonal symmetry irrespectively of the temperature of the measurement (down to $T = 4$ K). The HF structure consisted of two line pairs with about 1:3 intensity ratio when the magnetic field was aligned along [0001]. However, unlike for V_C^+ at the cubic site, the HF principal direction of the basal radicals of $V_C^+(h)$ strongly deviated from the perfect tetrahedral angle, and shifted from 103 down to 98° as the temperature was lowered from 150 to 10 K. This behavior was interpreted as an increase of the antibonding character between the axial and basal radicals when the temperature was lowered [27].

Most observations described above were accounted for by density-functional calculations. They arrived at ground state structures and HF tensors compatible with the low-temperature EPR data [22,23,28]. According to the calculations, $V_C^+(k)$ and $V_C^+(h)$ defects adopt C_{1h} and C_{3v} geometries in the ground state, with their highest (semi-)occupied Kohn-Sham states (HOKS) possessing a' and a_1 symmetry, respectively. Within the above LCAO picture they can be approximately described as $|a'\rangle \sim |11\bar{1}\bar{1}\rangle$ and $|a_1\rangle \sim |3\bar{1}\bar{1}\bar{1}\rangle$, respectively, explaining the HF structure observed for $V_C^+(k)$ and $V_C^+(h)$ at low-temperatures (~5K). They are also consistent with the measurements of $V_C^+(k)$ at $T > 50$ K if we assume that above this temperature the defect assumes a motional-averaged

trigonal state due to fast hopping between all three $|11\bar{1}\bar{1}\rangle$, $|1\bar{1}1\bar{1}\rangle$, and $|1\bar{1}\bar{1}1\rangle$ degenerate structures neighboring the undistorted (C_{3v}) configuration. Note that in line with the observations, all Si radicals contribute to $|a'\rangle$ in $V_C^+(k)$ (under static and dynamic conditions), and the amplitude of the axial radical ϕ_1 in the $|a_1\rangle$ state accounts for about 50% of the total LCAO localization in $V_C^+(h)$. The $|a_1\rangle$ paramagnetic state of $V_C^+(h)$ is also consistent with the observed antibonding character between Si_1 and the basal $Si_{2\text{-}4}$ radicals. However, the model is still unable to account for the magnitude of the high-temperature ($T > 30$ K) HF signals. Another puzzle, which was noted by Bockstedte and co-workers [22], is that despite being a singlet state, the trigonal $V_C^+(k)$ configuration is unstable against monoclinic distortion, implying the influence of a pseudo-Jahn-Teller (pJT) effect. However, neither was a justification provided for its manifestation, nor was it found why a similar effect is apparently missing in $V_C^+(h)$.

Negatively charged carbon vacancies were observed by EPR in n-type 4H-SiC irradiated either with MeV electrons at 850 °C or with 250 keV electrons at room temperature [10,29]. Although some traces of $V_C^-(k)$ and $V_C^-(h)$ signals could be detected above $T \approx 100$ K in darkness (in heavily doped material) [10], most experiments were performed on illuminated samples, which gave rise to much stronger signals [10,29,30]. At the cubic site and below $T \approx 40$ K, the $V_C^-(k)$ main line showed a monoclinic pattern and a single HF pair related to two symmetry-equivalent Si nuclei ($Si_{3,4}$) [30]. Additional and weaker HF signals were related to more distant shells. Above $T \approx 40$ K, the $Si_{3,4}$ HF signal disappeared from the spectrum and the main line acquired a trigonal pattern, accompanied by the appearance of a new axial HF pair (due to interaction between a magnetic Si_1 nucleus and the electron spin). As the temperature further increased, the magnitude of the Si_1 HF splitting increased and at ∼80-90 K a weak and broad HF pair accounting for three equivalent ($Si_{2\text{-}4}$) nuclei appeared in the spectrum as well [30]. Regarding $V_C^-(h)$, the main signal is monoclinic at $T = 60$ K and below. At these temperatures two HF signal pairs related to two inequivalent Si nuclei (Si_1 and Si_2) with C_{1h} site symmetry were detected. Raising the temperature above $T \sim 70$ K led to the broadening and disappearance of the Si_2 HF, while the main-line and Si_1 HF components merged into single trigonal peaks. The activation barrier for the monoclinic-trigonal conversion was estimated as 0.02 eV [29]. Within the temperature range of 70–120 K only the Si_1 HF was detected, but when $T > 120$ K a trigonal HF signal representative of three equivalent Si nuclei ($Si_{2\text{-}4}$) was also observed.

Again, first-principles modeling played a key role in grasping several of the above features [29–31]. Recent density functional calculations indicated that $V_C^-(k)$ has a $|a''\rangle \sim |00\bar{1}1\rangle$ paramagnetic ground state, whereas the symmetric $|a'\rangle \sim |1\bar{1}00\rangle$ state was metastable by only 0.03 eV [30]. The calculated HF tensors for $Si_{3,4}$ radicals accounted very well for the low-temperature ($T = 30$ K) experimental data. The quenching of the $Si_{3,4}$ HF signal above 40 K and the observation of trigonal hyperfine structures at higher temperatures was suggested to result from the partial population of both $|a''\rangle$ and $|a'\rangle$ states. Accordingly, under these conditions they would quickly hop between three equivalent Jahn-Teller (JT) distorted alignments. While this picture aims at accounting for the observed nonzero amplitude of the wave function on all four radicals above 90 K, it cannot be correct. Any sequential transformation between $|a'\rangle$ and $|a''\rangle$ states involves an intermittent quenching of the spin-density on the basal nuclei. Further, the model could not explain why there is a ∼40 K gap between the quenching of the $Si_{3,4}$ HF signal (at 40 K) and the appearance of the $Si_{2\text{-}4}$ HF signal (at 80 K). Also puzzling and unexplored was the fact that the $V_C^-(k)$ ground state was found to be nodal (a''), which in principle has higher kinetic energy than the metastable state (a'). Finally, the symmetry lowering of $V_C^-(k)$ cannot simply be explained by the JT effect. In the perfect vacancy (C_{3v} symmetry), the four $Si_{1\text{-}4}$ radicals hybridize into a fully occupied valence state $|a_1\rangle \sim |1111\rangle$, and three gap states $|a_1\rangle \sim |3\bar{1}\bar{1}\bar{1}\rangle$, $|e'\rangle \sim |0\bar{2}11\rangle$ and $|e''\rangle \sim |00\bar{1}1\rangle$ to be populated with three electrons. We calculated these states for an undistorted (trigonal) vacancy at the k site using the same method of Ref. [30] and they are depicted in Fig. 1(b). The latter two are higher in energy and represent orthogonal components of a doublet which is split from $|a_1\rangle$ due to the internal crystal field. For the case of $V_C^-(k)$, the doublet becomes partially populated (with a single electron) and the JT effect is expected to split $(e'' + e')^{\uparrow}$ (within C_{3v}) into $(a''^{\uparrow} + a')$ (within C_{1h}), where the upward arrow stands for the paramagnetic electron. Now, while the first-principles results from Ref. [30] indicate that the metastable $|a'\rangle$ state has amplitude on Si_1, it is clear from Fig. 1(b) that a JT-split component $|e'\rangle \sim |0\bar{2}11\rangle$ cannot account for this feature.

Turning now to $V_C^-(h)$, the calculations arrived at a C_{1h} ground state rather different than that found for the cubic site, namely the unpaired electron was localized on the Si_1-Si_2 pair as $|a'\rangle \sim |1\bar{1}00\rangle$ [29,31]. The calculated HF tensor elements for both (inequivalent) Si_1 and Si_2 radicals agreed very well with the measurements below $T = 60$ K (both in magnitude and principal directions), providing compelling evidence for the correctness of the model. The disappearance of the Si_2 HF signal together with the conversion of the C_{1h}-symmetric Si_1 HF into a trigonal signal at $T > 70$ K was justified based on a thermal activated hopping between $|1\bar{1}00\rangle$, $|10\bar{1}0\rangle$, and $|100\bar{1}\rangle$ equivalent states, which preserves a steady wave function amplitude only on Si_1 [29]. Again, the reasoning for a 70–120 K temperature window where only Si_1 HF was observed and above which another trigonal $Si_{2\text{-}4}$ HF was observed, was left unaddressed. Analogously to the metastable structure in the cubic site, the electronic structure of $V_C^-(h)$ in the ground state involves a nonvanishing spin-density on Si_1. Hence, unlike suggested in Ref. [29], the model cannot be explained by the JT effect, simply because none of the e-components in Fig. 1(b) shows nonzero amplitude on Si_1. Finally, $V_C^-(k)$ and $V_C^-(h)$ show monoclinic ground-states with opposite symmetry with respect to the mirror plane. Although the calculations were successful in accounting for the observed site-dependent ordering of electronic states [29,31], again the reasonings behind this effect were left unaddressed.

The connection of V_C (via EPR) with the $Z_{1/2}$ and $EH_{6/7}$ traps (via DLTS) was suggested based on the correlation between the position of the DLTS levels and the photo-EPR excitation thresholds for $V_C^{=} \rightarrow V_C^- + e^-$ and $V_C^0 \rightarrow V_C^+ + e^-$, respectively (where e^- represent a free electron at the conduction band bottom) [10]. More recently, Kawahara

et al. [32,33] investigated samples irradiated by low-energy (250 keV) electrons, which could displace C atoms only. In those works they reported a good correlation between the area density of EPR active V_C^- and the fraction of carriers trapped by the dominant $Z_{1/2}$ on samples irradiated with different electron fluences.

It seems clear that $Z_{1/2}$ is a negative-U center. This is consistent with the need of optical excitation in order to observe negatively charged vacancies by EPR. However, that is not the case for the defect responsible for $EH_{6/7}$. In recent state-of-the-art electrical level calculations using many-body perturbation [34] and hybrid density functional [35] methods, the donor levels were predicted to be separated by a small positive or essentially zero U-value ($U \approx 0.0$–0.2 eV). While this agrees with the low-temperature EPR measurements in darkness, it is also in apparent conflict with the negative-U ordering reported for EH_7 and tentatively proposed for EH_6 from DLTS [17]. As a word of caution, we note that when periodic charge corrections were neglected, the calculations clearly indicated $U < 0$ for both acceptors and donors [30,31,34].

It is clear that despite many advances, there are several fundamental puzzles to be solved. This paper aims at addressing those issues, as well as others that will become evident further ahead. In this section we wanted to introduce the reader to the main properties of the carbon vacancy in 4H-SiC, how the EPR data has been related to the prominent $Z_{1/2}$ and $EH_{6/7}$ electron traps, and the importance of theory/computational modeling in providing models and checking their quality. We will now proceed with a description of the theoretical methods followed by the main results. These include the reproduction of structures and electronic levels previously reported, as well as new results like a physical description of the observed pseudo-Jahn-Teller distortions, the crystal-field impact on the distinct electronic structure of cubic and hexagonal vacancies, and the atomistic mechanisms behind the T-dependent dynamic effects observed by EPR. Before the conclusions, we also include a section where we discuss the above issues.

II. THEORY

The calculations were carried out using the VASP package [36–39], employing the projector-augmented wave (PAW) method to avoid explicit treatment of core electrons [40]. A plane-wave basis set with kinetic energy up to 400 eV was used to describe the electronic Kohn-Sham states. The many-body electronic potential was evaluated using the hybrid density functional of Heyd-Scuseria-Ernzerhof (HSE06) [41,42], which mixes semilocal and exact exchange interactions at short ranges, treating the long-range interactions within the simpler generalized gradient approximation as proposed by Perdew, Burke, and Ernzerhof (PBE) [43]. When compared to plain PBE calculations, HSE06 has the main advantage of predicting a Kohn-Sham (indirect) band gap of 3.17 eV wide for 4H-SiC, which should be compared to the experimental value of 3.27 eV [44]. To a large extent, this approach mitigates the well known underestimated gap *syndrome* affecting PBE-level calculations, which show a 2.19 eV band-gap width. Although most results reported below were obtained using the HSE06 method, PBE-level results are also included and in that case they are explicitly identified.

We used 576-atom hexagonal supercells, obtained by replication of $6\times6\times2$ unit cells, from where a carbon atom was removed to produce a V_C defect. The equilibrium (calculated) lattice parameters of 4H-SiC were $a = 3.071$ Å and $c = 10.052$ Å. These are close to the experimental values of $a = 3.081$ Å and $c = 10.085$ Å extrapolated to $T = 0$ K [45]. All defect structures were optimized within PBE-level, using a conjugate-gradient method until the forces acting on the atoms were lower than 10 meV/Å. After this step, we took the relaxed structure, and self-consistent energies, electron and spin densities were finally obtained within HSE06. Electronic relaxations were computed with a numerical accuracy of 1 μeV, and the band structures were solved at $\mathbf{k} = (0\,0\,1/2)$ in reciprocal lattice units. This is conventionally referred to as the A point in the hexagonal Brillouin zone (BZ). We found this particular $\mathbf{k}$ point to provide the best compromise between sampling accuracy and computational performance. It is representative of the $\mathbf{k}$-point set $(0\,0\,\pm1/2)$ in nonrelativistic calculations, it led to energy differences with an error bar of about 5 meV (when compared to results obtained using $2\times2\times2$ sampled BZ), and most importantly, it did not cause so strong hybridization between defect levels lying high in the gap and the conduction band states as in the Γ-sampled PBE calculations of Ref. [30].

The above two-step recipe to obtain hybrid density-functional energies using structures that were previously relaxed within PBE (hereafter referred to as *pseudo-relaxed energies*), casts doubts regarding its accuracy when compared to *fully-relaxed* HSE06-energies obtained by minimizing HSE06-forces. To clarify this issue, we compared energies and forces of pseudo- and fully-relaxed $V_C^{++}(k)$ and $V_C^{=}(k)$ states. These two charge states have rather different structures (to be discussed below), and while $V_C^{++}(k)$ does not have electrons occupying gap levels, $V_C^{=}(k)$ has two fully occupied gap states, one of them being close to the conduction band edge. These tests were carried out using 256-atom supercells ($4\times4\times2$ unit cells) with a Γ-centered grid of 2^3 $\mathbf{k}$ points for BZ sampling. Accordingly, we obtained fully-relaxed HSE06-energies 13 meV and 11 meV below the energy of pseudo-relaxed $V_C^{++}(k)$ and $V_C^{=}(k)$ calculations, respectively. Despite these small relaxation energies, the average HSE06 force acting on $Si_{1\text{-}4}$ atoms on PBE-relaxed structures were 0.28 eV/Å and 0.10 eV/Å for for $V_C^{++}(k)$ and $V_C^{=}(k)$, respectively, and therefore cannot be neglected. However, the energy difference $E(q=-2) - E(q=+2)$ was 39.384 and 39.386 eV for pseudo-relaxed and fully-relaxed calculations, respectively, suggesting that the error of pseudo-relaxed energy differences is of the order of a few meV.

The energy of a charged defect, when calculated using periodic boundary conditions, is actually the energy of a supercell contaminated by artificial Coulomb interactions across an array of charged defects embedded on a compensating background charge [46]. These interactions are long-ranged and difficult to remove. Several *post-processing* recipes have been proposed to mitigate this problem (see, for example, Ref. [47] and references therein). Here we use the method by Freysoldt, Neugebauer, and Van de Walle [48], recently generalized for anisotropic materials [49]. Accordingly, the

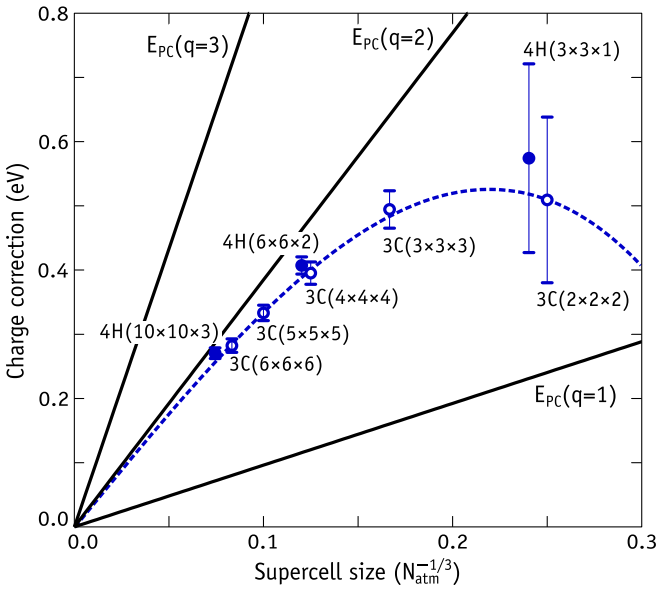

FIG. 2. Variation of the charge correction, $E_{\rm corr}$, obtained for a double positively charged carbon vacancy in 4H-SiC (closed circles) and 3C-SiC (open circles) supercells sized by the number of atoms, $N_{\rm atm}$. Error bars are standard deviations obtained from the averaging of $\Delta\bar{\phi}_{\rm PC,ind}$ [see Eq. (1)]. Integer triplets ($l \times m \times n$) are scaling factors applied to the lattice vectors of each unit cell to obtain the respective supercell. The dashed line represents a function of the form $aN_{\rm atm}^{-1} + bN_{\rm atm}^{-1/3}$ fitted to the data. Solid lines represent simple point charge corrections for $q = 1$, 2, and 3.

total energy of a defect in an *infinite* crystal is approximately $E_{\rm def}(q) \approx \tilde{E}_{\rm def}(q) + E_{\rm corr}(q)$, where q is a localized net charge on the defect, $\tilde{E}_{\rm def}$ is the total energy of the periodic problem and $E_{\rm corr}$ the charge correction,

$$E_{\rm corr}(q) = E_{\rm PC}(q) - q\,\Delta\bar{\phi}_{\rm PC,ind}(q), \tag{1}$$

where $E_{\rm PC}(q)$ is a point charge correction, which for isotropic materials reduces to the Madelung energy $E_{\rm PC,iso}(q) = \alpha_{\rm M} q^2/2\epsilon L$ and depends on the ratio between the Madelung constant $\alpha_{\rm M}$ and a characteristic length L (usually a lattice constant), the net charge and the dielectric constant ϵ. Further details about the explicit calculation of $E_{\rm PC}(q)$ for anisotropic materials (like 4H-SiC) can be found in Ref. [49].

$$\Delta\bar{\phi}_{\rm PC,ind}(q) = \bar{\phi}_{\rm ind}(q) - \bar{\phi}_{\rm PC}(q) \tag{2}$$

is the offset between the defect induced average potential $\bar{\phi}_{\rm ind}(q) = \bar{\phi}_{\rm def}(q) - \bar{\phi}_{\rm bulk}$ and that produced by a point charge, $\bar{\phi}_{\rm PC}(q)$ [49]. The space-averaged potentials $\bar{\phi}_{\rm def}$ and $\bar{\phi}_{\rm bulk}$ are obtained from first-principles from the Hartree (electrostatic) potential considering defective and pristine (bulk) supercells. The averaging is done at remote locations from the defect, more precisely at all atomic sites outside the largest sphere inscribed by the Wigner-Seitz supercell (see Fig. 2(a) of Ref. [49]). For the 576-atom supercell employed in this work, that meant a 15.1-Å radius sphere leaving a total of 382 outer atomic sites to be sampled.

Since defects distort and polarize the surrounding lattice, besides the electronic (ion-clamped) component, $\boldsymbol{\epsilon}_\infty$, the dielectric tensor employed in the calculation of $E_{\rm corr}$ has to account for the ionic contribution as well, $\boldsymbol{\epsilon} = \boldsymbol{\epsilon}_\infty + \boldsymbol{\epsilon}_{\rm ion}$ [47]. We calculated $\boldsymbol{\epsilon}_\infty$ using density-functional perturbation theory with local field effects within PBE [50]. The ionic part was evaluated from the Born effective charges and eigenfrequencies of the Hessian matrix [51]. Accordingly, we obtained $\epsilon^{\parallel} = 10.65$ and $\epsilon^{\perp} = 9.88$ for the dielectric constant parallel and perpendicular to the crystallographic c axis. These figures account well for the values $\epsilon^{\parallel} = 10.03$ and $\epsilon^{\perp} = 9.66$ obtained from refractive index measurements and Raman scattering data [52].

Figure 2 depicts the values of $E_{\rm corr}$ obtained for a $V_{\rm C}^{++}$ defect in 4H-SiC (with C_{3v} symmetry) and 3C-SiC (with T_d symmetry) as a function of the number of atoms in the supercell ($N_{\rm atm} \sim L^3$). The calculations shown in this particular figure were carried out within PBE-level. The results were essentially the same when using the HSE06 functional. Integer triplets in the figure ($l \times m \times n$) are scaling factors applied to the lattice vectors of the conventional cell (eight atoms in both polytypes) to obtain the respective supercell. For example, the largest hexagonal cell (4H-SiC) consisted of $(10 \times 10 \times 3) \times 8 = 2400$ atoms, whereas the smallest cubic cell (3C-SiC) had $(2 \times 2 \times 2) \times 8 = 64$ atoms. $E_{\rm corr}$ can be expanded in a power series of L, with the first term $E_{\rm PC} \sim L^{-1}$ and the second term scaling as L^{-3} [46,53]. The data were therefore used to fit a function of the form $aN_{\rm atm}^{-1} + bN_{\rm atm}^{-1/3}$, which is shown by the dashed line. The solid straight lines represent the leading term, $E_{\rm PC}(q = 1,2,3)$, as a function of $N_{\rm atm}$. It is clear that the simple Madelung (point-like) correction overestimates the spurious Coulomb energy. Also as expected, $E_{\rm corr}$ asymptotically converges to $E_{\rm PC}$ for supercells of infinite size. The error of the Madelung correction is always above the statistical error of $E_{\rm corr}$ obtained from averaging $\Delta\bar{\phi}_{\rm PC,ind}$ and shown as error bars. In the case of the 4H-SiC ($6 \times 6 \times 2$) supercells (used in this work to study the carbon vacancy), our best estimate for the correction of $V_{\rm C}^{++}$ is $E_{\rm corr}(q = 2) = 0.41 \pm 0.01$ eV, whereas for a singly charged vacancy (not shown in the graph) we obtained $E_{\rm corr}(q = 1) = 0.10 \pm 0.01$ eV.

For the calculation of formation energies we follow the usual procedure, introduced by Qian, Martin, and Chadi [54]. Here the formation energy of a carbon vacancy is

$$E_{\rm f}(q,R,\mu_{\rm C},E_{\rm F}) = E_{\rm def}(q,R) - E_{\rm bulk} + \mu_{\rm C} + q(E_{\rm v} + E_{\rm F}), \tag{3}$$

where $E_{\rm def}$ is the charge-corrected total energy of the defective supercell as defined above. Besides depending on the charge state q, $E_{\rm def}$ may refer to more than one atomic structure R. $E_{\rm bulk}$ is the energy of a perfect supercell, $\mu_{\rm C}$ is the carbon chemical potential (see below), $E_{\rm v}$ is the valence band edge and $E_{\rm F}$ the Fermi energy which may vary within $E_{\rm F} = [0, E_{\rm g}]$. The upper limit, $E_{\rm g} = I_{\rm bulk} - A_{\rm bulk} = 3.42$ eV, is the calculated forbidden gap width, here obtained within the delta self-consistent (ΔSCF) method [55], where $A_{\rm bulk} = E_{\rm bulk}(0) - E_{\rm bulk}(-1) = -11.03$ eV and $I_{\rm bulk} = E_{\rm bulk}(+1) - E_{\rm bulk}(0) = -7.61$ eV are ionization potentials of neutral and negatively charged supercells. They are negative as their reference (zero-energy) is ill-defined for a periodic calculation. According to this method $E_{\rm v} = -I_{\rm bulk}$, allowing to consistently express the calculated transition levels with respect to both $E_{\rm c}$ and $E_{\rm v}$ without having to rely on the experimental band gap.

We note that using the A point for BZ sampling, the $E_g = 3.42$ eV obtained by the ΔSCF method is 0.25 eV wider than the indirect gap from the Kohn-Sham energies of the highest-occupied and lowest-unoccupied states at $\mathbf{k} = \Gamma$ and $\mathbf{k} = M = (1/2\,0\,0)$, respectively. This compares with $E_g = 3.15$ and 3.25 eV from analogous ΔSCF calculations using Γ-centered $1 \times 1 \times 1$ (simple Γ-point) and $2 \times 2 \times 2$ $\mathbf{k}$-point sampling grids. The Γ-sampled E_g energy coincides with the Kohn-Sham gap simply because of band-folding, which for a $6 \times 6 \times 2$-supercell brings the M point into the origin of the BZ. These results indicate that $1 \times 1 \times 1$-sampled energy differences (like Γ- and A-point calculations) may suffer from insufficient sampling density. This effect is expected to be more severe for energy differences involving the occupation (or emptying) of highly dispersive states. The calculation of $I_{\text{bulk}} - A_{\text{bulk}}$ is perhaps an extreme case. It involves emptying the top-most valence band and filling the bottom-most conduction band, both showing considerable dispersion amplitudes. On the other hand, for sufficiently large supercells, localized defect states show little dispersion and sampling errors tend to cancel when considering energy differences. This is confirmed by Γ-point, A-point, and $2 \times 2 \times 2$-grid calculations of $E_{\text{def}}(q = -2) - E_{\text{def}}(q = +2)$ for the vacancy at the k site, which gives an average value and maximum deviation of 39.480 ± 0.003 eV.

In Eq. (3), μ_C represents the energy per carbon atom in the SiC crystal, which is subject to

$$\mu_C^0 + \Delta H_{\text{SiC}}^{\text{f}} \leqslant \mu_C \leqslant \mu_C^0, \tag{4}$$

where the upper and lower bounds represent C-rich and C-poor SiC crystals, which are in equilibrium with standard carbon and silicon phases, respectively. For crystals grown under stoichiometric conditions we have $\mu_C = \mu_C^0 + \Delta H_{\text{SiC}}^{\text{f}}/2$. Here, $\Delta H_{\text{SiC}}^{\text{f}}$ is the heat of formation of SiC estimated as $\Delta H_{\text{SiC}}^{\text{f}} = \mu_{\text{SiC}}^0 - \mu_C^0 - \mu_{\text{Si}}^0 = -0.62$ eV, with μ_{SiC}^0 being the energy per SiC formula unit in a perfect crystal, while μ_C^0 and μ_{Si}^0 are *standard* chemical potentials (energy per atom) of C and Si in diamond and silicon crystals, respectively. The value calculated for $\Delta H_{\text{SiC}}^{\text{f}}$ is close to -0.72 eV as obtained from calorimetry measurements [56].

An important use of Eq. (3) is in locating the value of E_F for which two different charge states, say q and $q+1$, have the same energy, and therefore the same probability to occur. The $(q/q+1)$ transition level with respect to the valence band top is found at $E_F = E(q/q+1) - E_v$ such that $E_f(q, R_q, \mu_C, E_F) = E_f(q+1, R_{q+1}, \mu_C, E_F)$,

$$E(q/q+1) - E_v = [E_{\text{def}}(q, R_q) - E_{\text{def}}(q+1, R_{q+1})] - I_{\text{bulk}}, \tag{5}$$

where we distinguish eventual different structures R_q and R_{q+1} for charge states q and $q+1$, respectively. It is also useful to calculate transition levels with respect to the conduction band minimum. For that we have

$$E_c - E(q/q+1) = A_{\text{bulk}} - [E_{\text{def}}(q, R_q) - E_{\text{def}}(q+1, R_{q+1})]. \tag{6}$$

We also investigated the transformation of V_C defects between different structures and also between different symmetry-equivalent alignments. We assume the adiabatic approximation, and the potential energy surface governing the atomic motion was calculated using the climbing-image nudged elastic band (NEB) method [57]. The NEB algorithm allows to find saddle points and minimum energy paths separating known initial and final structures. The method optimizes a number of intermediate structures along the reaction path while maintaining equal *spacing* between them. This is possible thanks to the introduction of spring forces connecting neighboring structures (the elastic band) and projecting out the component of the force due to the potential perpendicular to the band. The NEB relaxations were carried out within the PBE-level, used seven intermediate structures, and the forces acting on the atoms were also converged within 0.01 eV/Å. The initial, final, and saddle-point structures (R_i, R_f, and R_{sp}, respectively) were used to obtain their respective total energies (E_i, E_f, and E_{sp}) using the HSE06 functional.

III. RESULTS

A. Ground-state results for the carbon vacancy

We start by reporting on the structural properties of the defect on different charge states. The V_C defect was always found to have the lowest energy in low-spin states. We identified four different atomistic configurations, which we label with the letters A (with C_{3v} symmetry), and B, C, and D (with C_{1h} symmetry). They are distinguished by the shape of the tetrahedron with volume v and with edge lengths x_{ij} connecting Si_i-Si_j nuclei. Some edges are shorter/longer than others and they are schematically represented by solid/dashed edges, respectively, in the middle of Fig. 3. By defining an effective length as the geometric average length of the edges $\bar{x} = (6\sqrt{2}v)^{1/3}$, A–D structures may be defined by simple distortion coordinates $\mathbf{Q}_{\text{A-D}}$ with magnitudes,

$$Q_A = +3\delta x_{12} - 3\delta x_{34}, \tag{7}$$

$$Q_B = -\delta x_{12} + 2\delta x_{13} + 2\delta x_{23} - \delta x_{34}, \tag{8}$$

$$Q_C = +\delta x_{12} + 2\delta x_{13} + 2\delta x_{23} - \delta x_{34}, \tag{9}$$

$$Q_D = -\delta x_{12} + 2\delta x_{13} - 2\delta x_{23} + \delta x_{34}, \tag{10}$$

where $\delta x_{ij} = x_{ij} - \bar{x}$ elongations have pre-factors that depend on the number of symmetry-equivalent edges. Hence structure A forms a triangular pyramid with a Si_1 apex and a contracted $\text{Si}_{2\text{-}4}$ base, whereas structures B, C, and D form monoclinic tetrahedrons with a $(\bar{1}010)$ mirror plane and mirror-symmetric Si_3 and Si_4. On these three structures, we found 2, 1, and 3 contracted edges (4, 5, and 3 elongated ones), respectively. Below, we show how these shapes are intimately related to the occupation of the one-electron orbitals.

In line with previous works [22,23,28,30,31], we found that $V_C^{++}(k)$ and $V_C^{++}(h)$ defects are trigonal (structure A). Both introduce three empty states deep in the gap, namely a singlet level below a doubly degenerate level ($a_1 + e$). Their separation Δ_{xf} results from the local crystal field. Figure 3 represents the (hybrid) Kohn-Sham energies of ground-state carbon vacancies as a function of the level occupancy and sublattice site. The level energies are reported with respect to the ϵ_{HOKS} eigenvalue of bulk. To make the interpretation

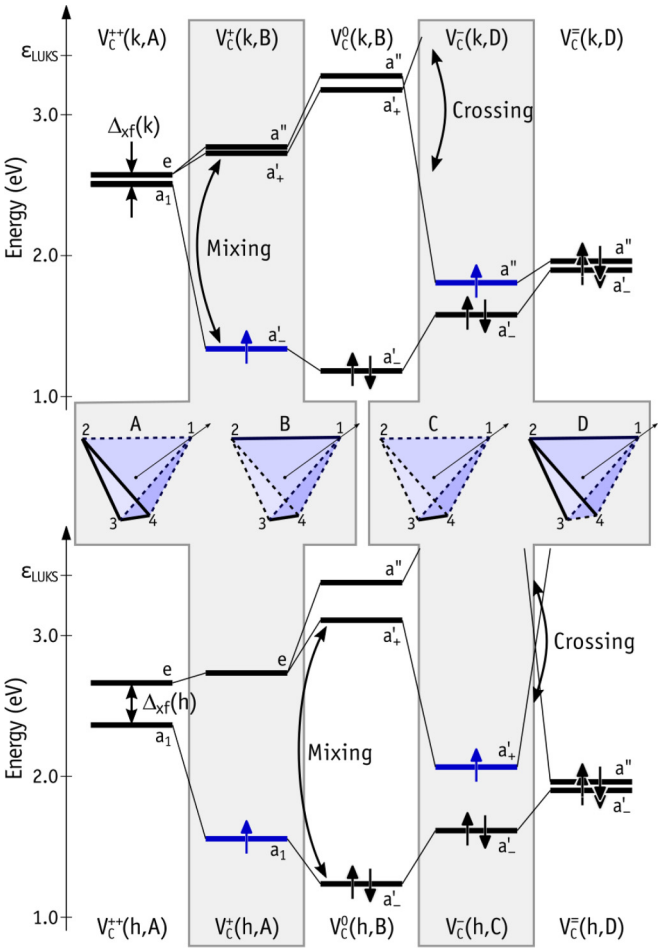

FIG. 3. Kohn-Sham electronic states at $\mathbf{k} = (0\,0\,1/2)$ for the carbon vacancy at the cubic (upper half) and hexagonal (lower half) sites. The zero of the energy scale is at the ϵ_{HOKS} energy in bulk (using the HSE06 functional). Electrons are represented by upward (spin-up) and downward (spin-down) arrows. Each state is accompanied by symmetry labels (see text for details). The central region displays the structures found for positively charged (A and B) and negatively charged (C and D) defects. Contracted/elongated Si-Si distances are represented as solid/dashed lines, respectively.

easier, we present a spin-averaged picture, although the filling of levels is represented with upward/downward arrows.

From the eigenvalues, we obtain crystal-field energies $\Delta_{xf}(k) = 0.06$ and 0.30 eV for $V_C^{++}(k)$ and $V_C^{++}(h)$, respectively. We will show that this site-dependence of the crystal-field confers rather distinct electronic structures on $V_C(k)$ and $V_C(h)$. Table I reports the geometrical details regarding the evolution of ground-state structures as we fill in the $a_1 + e$ manifold with electrons. Also included are the results for metastable structures (starred structures). These were only found for $q = \pm 1$ charge states and will be discussed in Sec. III B. Besides edge elongations δx_{ij}, distortion magnitudes Q_R and the volume expansion $\delta v = v - v_{bulk}$ of the vacancy tetrahedron (with respect to the analogous quantity in bulk) are also shown. It is clear that positive charge states are compressive ($\delta v > 0$), while negatively charged ones are tensile ($\delta v < 0$). This is a consequence of the breaking/formation of reconstructed bonds between

TABLE I. Structural details of four structure types (R = A, B, C, and D) found for the carbon vacancy in 4H-SiC on different sublattice sites ($s = k, h$) and charge states ($-2 \leqslant q \leqslant +2$). Structures are specified by their edge length variations δx_{ij} (in angstroms), volume expansion δv (in Å^3) and distortion magnitude Q_R (in Å). Starred structures are metastable. See text for detailed definitions.

(s,q)	R	δx_{12}	δx_{13}	δx_{23}	δx_{34}	δv	Q_R
(k, ++)	A	0.032	0.032	−0.031	−0.031	0.626	0.191
(k,+)	A*	0.061	0.061	−0.058	−0.058	0.140	0.359
(k,+)	B	−0.117	0.090	0.035	−0.093	0.090	0.461
(k,0)	B	−0.241	0.180	0.139	−0.200	−0.443	1.079
(k,−)	C*	0.000	0.111	0.112	−0.309	−0.679	0.747
(k,−)	D	−0.312	0.267	−0.090	0.141	−0.716	1.167
(k,=)	D	−0.233	0.345	−0.234	0.359	−1.065	1.750
(h,++)	A	0.006	0.006	−0.006	−0.006	0.581	0.036
(h,+)	A	0.061	0.061	−0.061	−0.061	0.196	0.366
(h,+)	B*	−0.065	0.088	0.000	−0.102	0.132	0.335
(h,0)	B	−0.229	0.146	0.097	−0.256	−0.440	0.971
(h,−)	C	0.037	0.097	0.068	−0.367	−0.640	0.735
(h,−)	D*	−0.071	0.194	−0.286	0.255	−0.703	1.286
(h,=)	D	−0.220	0.295	−0.331	0.292	−1.033	1.765

the four Si radicals edging the vacancy as we respectively remove/add electrons from/to defect states in the gap. For the same reason, distortions (Q_R) tend to increase in magnitude as we go from V_C^{++} to $V_C^{=}$. We also note that structures A and B were concurrently found for the positive charge state, whereas structures C and D were found for the negative charge state. This is emphasized in Fig. 3 by two shaded regions.

All paramagnetic ground-states differ in their atomic geometries, namely $V_C^{+}(k,B)$, $V_C^{+}(h,A)$, $V_C^{-}(k,D)$, and $V_C^{-}(h,C)$, and show C_{1h}, C_{3v}, C_{1h}, and C_{1h} symmetry, respectively. Inspection of the paramagnetic (highest occupied) one-electron wave functions allowed us to identify their symmetry and LCAO representations. For the monoclinic structures we have two mirror-symmetric a' states (see Fig. 3), and they are distinguished by $-$ and $+$ subscripts, standing for low- and high-energy symmetric states. Hence we found that $|a'_-\rangle \sim |11\bar{1}\bar{1}\rangle$ and $|a_1\rangle \sim |3\bar{1}\bar{1}\bar{1}\rangle$ for $V_C^{+}(k,B)$ and $V_C^{+}(h,A)$, respectively, while for negative charge states we found $|a''\rangle \sim |00\bar{1}1\rangle$ and $|a'_+\rangle \sim |1\bar{1}00\rangle$ for $V_C^{-}(k,D)$ and $V_C^{-}(h,C)$, respectively. Besides being compatible with the low-temperature EPR and HF data, the above results reproduce earlier density-functional findings [22,23,28,30].

We went on and explored the symmetry and wave-function character of nonparamagnetic states. The results are shown in Fig. 3. Here we can see that the evolution of the one-electron states, as they become occupied, exhibits a rich picture, which includes crossing and mixing (anticrossing) features. These effects are responsible for the structural variety that is observed, and to understand them we have to invoke the JT and pJT effects.

B. The pseudo-Jahn-Teller effect on the carbon vacancy in 4H-SiC

While the JT theorem asserts the existence of spontaneous symmetry breaking of degenerate electronic states: "The

pJT effect is the only source of instability and distortions of high-symmetry configurations of polyatomic systems in nondegenerate states, and it contributes significantly to the instability of degenerate states" [58].

The pJT effect results in the softening of the adiabatic potential energy surface (APES) around a *reference configuration* 0 with nondegenerate ground state Ψ_0, and it is due to overlap with excited states via electron-phonon coupling. Should this softening be severe enough to make Ψ_0 unstable against atomic distortion towards structure R, the curvature of the APES along $\mathbf{Q}_R$, which transforms as some irreducible representation Γ_R, must be negative, $k^R = (\partial^2 E/\partial \mathbf{Q}_R^2)_0 < 0$. Here $E = \langle\Psi_0|\hat{H}|\Psi_0\rangle$ is the total energy and $\hat{H}$ the Hamiltonian. It may be shown [58,59] that the APES softening comes from a negative vibronic contribution $k_{\rm v}^R$ to the total curvature $k^R = k_0^R + k_{\rm v}^R$, where

$$k_0^R = \left\langle \Psi_0 \middle| \left(\frac{\partial^2 \hat{H}}{\partial \mathbf{Q}_R^2}\right)_0 \middle| \Psi_0 \right\rangle \tag{11}$$

is the harmonic curvature and from second-order perturbation theory,

$$k_{\rm v}^R = -2\sum_n \frac{|F_{0n}|^2}{E_n - E_0}, \tag{12}$$

where $F_{0n} = \langle\Psi_0|(\partial \hat{H}/\partial \mathbf{Q}_R)_0|\Psi_n\rangle$ are off-diagonal vibronic coupling constants between the reference state Ψ_0 and excited states Ψ_n with energies E_0 and E_n, respectively. k_0^R represents the force constant resisting the motion of atoms along $\mathbf{Q}_R$, whereas $k_{\rm v}^R$ is always negative and represents the change in that force constant that results from adapting the electron distribution to one more suited to the new nuclear coordinates,

$$\Psi_R = \Psi_0 - \sum_n \frac{F_{0n}}{E_n - E_0}\Psi_n, \tag{13}$$

corresponding to a lower energy E_R. We note that unlike the Jahn-Teller effect, the pJT effect mixes the ground state with excited states to create new bonds and distort the structure. We may actually state that the driving force of the pJT effect is the increase of covalent bonding [59].

Given that the product $(\partial \hat{H}/\partial \mathbf{Q}_R)\mathbf{Q}_R$, which is the linear term in the expansion of $\hat{H}$ in powers of $\mathbf{Q}_R$, is fully symmetric, $\partial \hat{H}/\partial \mathbf{Q}_R$ must also have the same symmetry as $\mathbf{Q}_R$. This implies that only excited states Ψ_n, which transform as the same irreducible representation of Ψ_0, such that $\Gamma_R = \Gamma_0 \otimes \Gamma_n$, will lead to nonvanishing F_{0n} coupling constants and contribute to the softening of the APES [60–62].

Besides the symmetry restrictions imposed to the F_{0n} integral, it is often assumed that only a few low-energy states contribute to $k_{\rm v}^R$ due to the increasing $E_n - E_0$ energy in denominator of Eq. (12) [63]. This premise has justified the replacement of the infinite sums in Eqs. (12) and (13) by a finite set of interacting states, or indeed by a two-level paradigm where a single excited state couples to the ground state via an effective vibronic coupling constant $k_{\rm v}^R = -F_{01}^2/\Delta$, where $2\Delta = E_1 - E_0$ is the effective energy separation between the mixing states [63].

For an accurate description of the pJT effect one would have to solve the many-body Hamiltonian by accounting for dynamic correlation effects (e.g., by means of configuration interaction methods), the electron-phonon coupling would have to be included as well, considering all phonons obeying the above selection rule. Although this has been realized for small molecules using sophisticated quantum chemistry methods [59], severe approximations have to be made in order to study defects in solids. By using a single-determinant density functional approach we may still arrive at a sufficiently detailed picture of the problem. For instance, García-Fernández and co-workers [64] were able to explain the off-center displacement of the Fe^+ interstitial ion in $SrCl_2$ using local density functional theory. On the contrary, the wave-function-based complete active space second-order perturbation method was applied to the same problem and was unable to reproduce the observations. This failure was attributed to the insufficient number of states included in the active space [64]. The case of a vacancy in SiC would be much more demanding since the active space spans many ligands to the vacancy site.

We investigated the pJT effect on the V_C defect in 4*H*-SiC, restricting our approach to a single-electron picture. Although we do not have access to important parameters such as accurate many-body gap energies and electron-phonon coupling strengths, we will arrive at an instructive and reasonable picture for the observed distortions. To that end we monitored the change of the one-electron wave functions and respective energies, while the atomic structure was progressively changed from the high-symmetry V_C(A) configuration towards lower-symmetry structures B, C, and D with C_{1h} symmetry ($\Gamma_R = A'$). Therefore, according to the selection rules, only fully symmetric states (a') have to be considered as the source of a pJT effect in V_C. The calculations reported within this Subsection were done using the spin-averaged density-functional method within the PBE level. Some tests using a spin-polarized HSE06 functional were also carried out, and apart from the expected differences regarding the energy separation of levels, the conclusions drawn below apply equally.

We begin with neutral and positively charged defects. On the left-hand side of Fig. 4, we depict the highest occupied and lowest unoccupied Kohn-Sham states (HOKS and LUKS, respectively) for the ground state neutral vacancy at the k site, $V_C^0(k,\mathrm{B})$. Both HOKS and LUKS transform according to the a' irreducible representation of the C_{1h} point group, so we differentiate them by their energy order, i.e., the one with lower energy is referred to as $|\mathrm{HOKS}\rangle = |a'_-\rangle$ while the higher energy state is $|\mathrm{LUKS}\rangle = |a'_+\rangle$. If we consider all three states in the gap, the electronic structure of $V_C^0(k,\mathrm{B})$ is $|a'^2_- a'_+ a''\rangle$, where the number of electrons on a specific orbital is superscripted. Comparing the ground state $|a'_-\rangle$ in Figure 4 with $|a_1\rangle$ from $V_C^0(k,\mathrm{A})$ shown in Fig. 1(b), it is evident that the lower symmetry state increases the covalent bonding between all four atoms, and that leads to shorter Si_1-Si_2 and Si_3-Si_4 distances in structure B. Furthermore, considering that $V_C^0(k,\mathrm{A})$ is a nondegenerate ground state ($|a_1^2\, e\rangle$), we conclude that the states exhibited in Fig. 4 must result from a pJT effect.

On the right-hand side of Fig. 4, we find an electronic structure diagram, showing how the three gap states develop

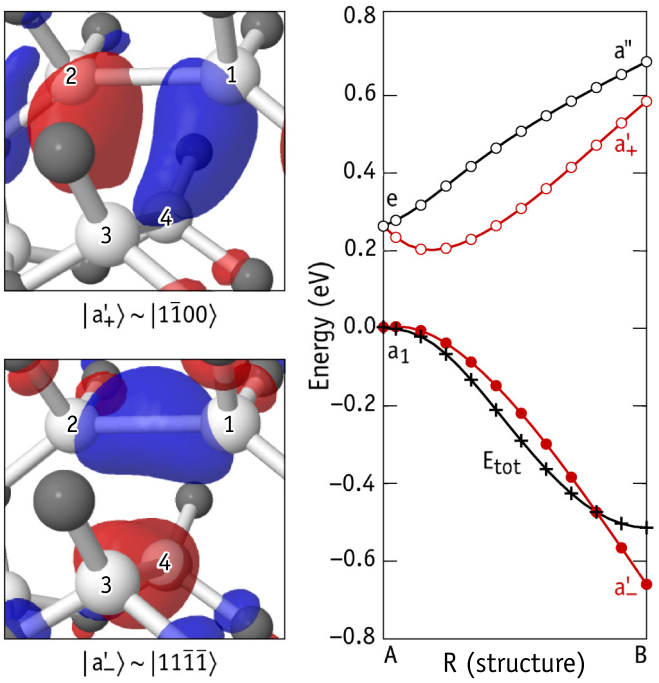

FIG. 4. (Left) Shape of the highest occupied and lowest unoccupied Kohn-Sham orbitals ($|a'_-\rangle$ and $|a'_+\rangle$, respectively) of $V_C^0(k,B)$ calculated at $\mathbf{k} = (0\,0\,1/2)$ within PBE-level. Blue and red isosurfaces correspond to positive and negative phases of the orbitals. (Right) Evolution of the Kohn-Sham energies in the gap as the structure distorts from $V_C^0(k,A)$ to the $V_C^0(k,B)$ ground state. Occupied and empty states are represented as solid and open circles, respectively. The total energy (E_{tot}) is shown as crosses. The origin for Kohn-Sham and total energies is ϵ_{HOKS} and E_{tot} at $R = A$, respectively. Symmetry labels are indicated for each state.

between the trigonal $V_C^0(k,A)$ state with electronic configuration $|a_1^2\, e\rangle$ and the monoclinic $V_C^0(k,B)$ state with electronic configuration $|a'^2_-\, a'_+\, a''\rangle$. Energies of filled and empty states are represented with closed and open symbols, respectively. The same graph also shows the total energy change as crosses, from which we conclude that the high-symmetry configuration A is unstable against relaxation to B. The corresponding *pseudo-Jahn-Teller relaxation energy*, $E_{pJT} = 0.5$ eV, relates to the added covalence. The $\mathbf{Q}_B$ distortion transforms as A' within C_{1h} (couples to a' electronic states), and consists in the compression of Si_1-Si_2 and Si_3-Si_4 distances, along with the expansion of the remaining tetrahedron edges (see Table I). Looking again at Fig. 1(b), it becomes evident that when subject to a $\mathbf{Q}_B$ distortion, the state $|a_1\rangle \sim |3\bar{1}\bar{1}\bar{1}\rangle$, which transforms as a' within C_{1h} and shows a strong antibonding character between Si_1-Si_2, should raise in energy, while the doublet component $|e'\rangle \sim |0\bar{2}11\rangle$, also transforming as a' within C_{1h} and showing a bonding character between Si_3-Si_4, is expected to be stabilized and lower its energy. This opposite coupling leads to the typical pJT *anticrossing* pattern shown in Fig. 4 for $|a'_-\rangle$ and $|a'_+\rangle$ states.

We may estimate the relative contribution (mixing) from $|a_1\rangle$ and $|e'\rangle$ states to the pJT distorted $|a'_-\rangle$ and $|a'_+\rangle$ states using our simple LCAO model. From inspection of Figs. 1(b) and 4, and considering normalization coefficients $|a_1\rangle = 12^{-1/2}\,|3\bar{1}\bar{1}\bar{1}\rangle$ and $|e'\rangle = 6^{-1/2}\,|0\bar{2}11\rangle$ we arrive at

$$|a'_+\rangle = (2/3)^{1/2}|a_1\rangle + (1/3)^{1/2}|e'\rangle = (1/2)^{-1/2}\,|1\bar{1}00\rangle, \quad (14)$$

$$|a'_-\rangle = (1/3)^{1/2}|a_1\rangle - (2/3)^{1/2}|e'\rangle = 1/2\,|11\bar{1}\bar{1}\rangle. \quad (15)$$

Like the isosurfaces shown in Fig. 4, the ground state $|a'_-\rangle$ in Eq. (15) has the same phase (bonding character) on $Si_{1,2}$ and $Si_{3,4}$ atom pairs, and that mostly comes from $|e'\rangle$. Conversely, $|a'_+\rangle$ is an antibonding state between $Si_{1,2}$ atoms with vanishing amplitude on $Si_{3,4}$, and most of its character comes from $|a_1\rangle$. The above discussion and conclusions can be applied to the neutral vacancy at the hexagonal site as well. However, the stronger crystal-field splitting leads to a larger energy gap $2\Delta = E_1 - E_0$, and therefore to a weaker mixing effect.

For positively charged vacancies on both k and h sites, the shape of the electronic structure diagrams (and wavefunctions) were found to be close to those of Fig. 4, although E_{tot} for $V_C^+(A)$ and $V_C^+(B)$ indicated that these were both minima in the APES of k and h sites. From Table I, we see that the distortion magnitudes of positively charged defects are considerably smaller than in neutral defects. We may conclude that the pJT coupling is weaker for $V_C^+(B)$, particularly in the hexagonal site where the crystal field is stronger. Here, the $V_C^+(h,B)$ state $|a'^1_-\rangle \sim |11\bar{1}\bar{1}\rangle$ with two (weak) Si-Si bonds sharing a single electron, is essentially degenerate with the $V_C^+(h,A)$ state $|a_1^1\rangle \sim |3\bar{1}\bar{1}\bar{1}\rangle$. Their energy difference is estimated below $E_{pJT} = 1$ meV.

For the negatively charged vacancies, the picture is dramatically different. We start by analyzing the double negative charge state, where structure D was found to be the most stable for both k and h sites. For the trigonal structure on the k site (the structure was relaxed by symmetrizing the forces), we found that the $|a_1^2 e^2\rangle$ state with spin-0 was less stable than the spin-1 configuration by 0.20 eV, but the latter was still metastable by 0.15 eV when compared to the $|e^4 a_1\rangle$ nondegenerate ground state. On the left-hand side of Fig. 5, we depict the (fully occupied) levels found within the gap for $V_C^=(k,D)$. Comparing these wave-functions with those shown in Fig. 1(b) for the symmetric structure, we realize that although the HOKS state $|a''\rangle$ of structure D is rather similar to $|e''\rangle \sim |00\bar{1}1\rangle$ from the trigonal structure, the $|a'_-\rangle$ does not find a good match, although one could suggest some resemblance with $|a_1\rangle$. Considering that (i) $V_C^=(k,A)$ is nondegenerate, and therefore not vulnerable to a JT distortion, and (ii) that $|a'_-\rangle$ is a mixed state with a major contribution from $|a_1\rangle$, the wave functions exhibited in Fig. 5 must result from a pJT effect. In fact, looking at the right-hand side of Fig. 5, it becomes evident that $|a_1\rangle$ has been converted into $|a'_-\rangle$ under distortion $\mathbf{Q}_D$, whereas $|a'_+\rangle$ (derived from e') seems to have merged into the conduction band (uppermost state close to 0.8 eV) before the ground state was attained.

In fact, $|a'_-\rangle$ shows bonding character for Si_1-Si_2 and Si_3-Si_4 pairs, and can be described approximately as $\sim|11\bar{1}\bar{1}\rangle$ like in Eq. (15). It becomes now clear that structure D results from structure B (occupation of $|a'_-\rangle$ leads to the shortening of Si_1-Si_2 and Si_3-Si_4 distances) combined with the occupation of $|a''\rangle$, which is antibonding on Si_3-Si_4. The result is a tetrahedral structure with short Si_1-Si_2, Si_2-Si_3, and Si_2-Si_4 edges. We

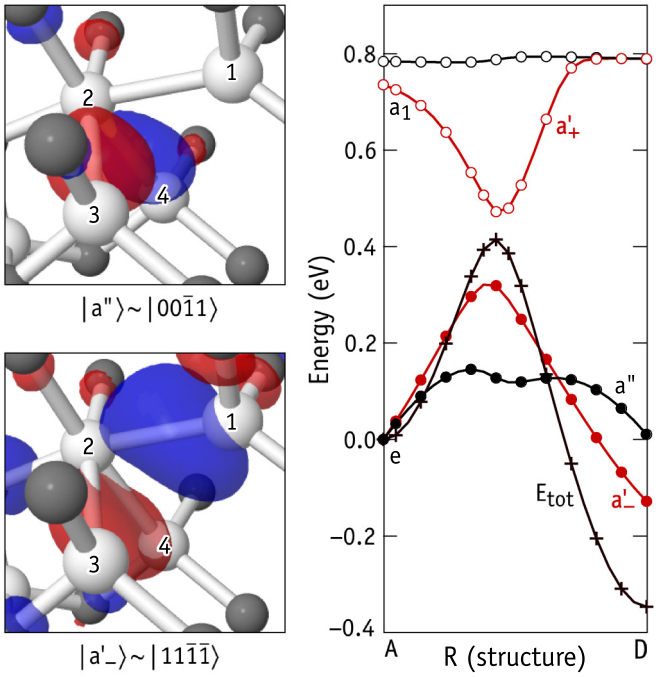

FIG. 5. (Left) Shape of the HOKS − 1 and HOKS orbitals ($|a'_-\rangle$ and $|a''\rangle$, respectively) of $V_C^=(k,D)$ calculated at $\mathbf{k} = (0\,0\,1/2)$ within PBE level. Blue and red isosurfaces correspond to positive and negative phases of the orbitals. (Right) Evolution of the Kohn-Sham energies in the gap as the structure distorts from $V_C^=(k,A)$ to the $V_C^=(k,D)$ ground state. Occupied and empty states are represented as solid and open circles, respectively. The total energy (E_{tot}) is shown as crosses. The origin for Kohn-Sham and total energies is ϵ_{HOKS} and E_{tot} at $R = A$, respectively. The topmost data points connected by a flat curve represent the conduction band bottom. Symmetry labels are indicated for each state.

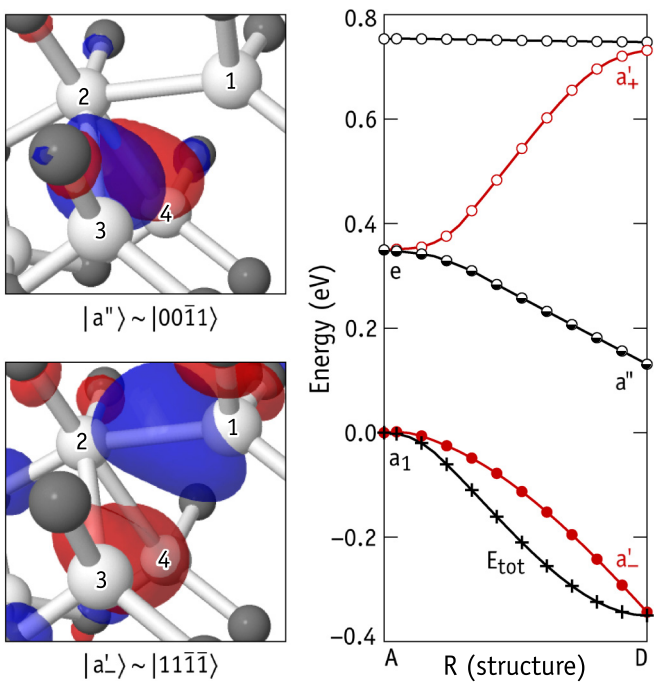

FIG. 6. (Left) Shape of the HOKS − 1 and HOKS orbitals ($|a'_-\rangle$ and $|a''\rangle$, respectively) of $V_C^-(k,D)$ calculated at $\mathbf{k} = (0\,0\,1/2)$ within PBE-level. Blue and red isosurfaces correspond to positive and negative phases of the orbitals. (Right) Evolution of the Kohn-Sham energies in the gap as the structure distorts from $V_C^-(k,A)$ to the $V_C^-(k,D)$ ground state. Occupied, semioccupied, and empty states are represented as solid, half-filled, and open circles, respectively. The total energy (E_{tot}) is shown as crosses. The origin for Kohn-Sham and total energies is ϵ_{HOKS} and E_{tot} at $R = A$, respectively. The topmost data points connected by a flat curve represent the conduction band bottom. Symmetry labels are indicated for each state.

finally note that $V_C^=(h)$ shows a similar behavior to $V_C^=(k)$, with the metastability of the trigonal structure by 0.5 eV being worthy of mentioning.

For the singly negative charge states, we found that imposing structure A to the defect (symmetry-constrained relaxation) the self-consistent electronic structure showed a $|a_1^2\, e^1\rangle$ occupation (with spin-1/2) for both sites h and k. In this case both trigonal structures are vulnerable to the JT effect. Monoclinic distortions applied to $V_C^-(k,D)$ and $V_C^-(h,C)$ ground states were found to release 0.39 and 0.36 eV, respectively. The two highest occupied states of $V_C^-(k,D)$ and their change along the A–D path on the APES are depicted in Fig. 6. We can conclude that despite showing occupied $|a'_-\rangle$ and $|a''\rangle$ states like in the double minus charge state (and hence showing a similar structure), the diagram on the right side of the figure is rather different than that shown in Fig. 5. The high-symmetry configuration $V_C^-(k,A)$ is now unstable due to the Jahn-Teller effect. Interestingly, the splitting order of the e-state favors the stabilization of the nodal a'' state with higher kinetic-energy (under the monoclinic field). We will come back to this issue in Sec. IV.

On the h site, we found that the JT splitting order of the e state of $V_C^-(h,A)$ involves the raising in energy of the antisymmetric state a'' under the monoclinic distortion $\mathbf{Q}_C$. Unlike for the cubic site, we have now a $|a'^2_-\, a'^1_+\, a''\rangle$ occupation scheme. This difference is attributed to the relatively stronger crystal field separating a_1 and e states of the symmetric configuration in $V_C^-(h)$, and consequently to a weaker coupling between $|a'_-\rangle$ and $|a'_+\rangle$ states. The resulting structure C is therefore based on structure B (due to the occupation of $|a'_-\rangle$), but shows an elongated Si_1-Si_2 distance due to occupation of the antibonding $|a'_+\rangle$ state (see Fig. 4).

C. Dynamical effects

We calculated minimum energy barriers separating different distorted structures along the APES using the NEB method. Table II reports the most favorable forward (E_{fwd}) and backward (E_{bak}) barriers, between several initial and final structures. The sublattice site and charge state are indicated as (s,q) pairs on the first column. Two types of mechanisms were considered, namely rotations (R) and transformations (T). A rotation involves a 120° *rotation* of the mirror plane of monoclinic structures (B, C, and D), which are converted into symmetry-equivalent final states (B′, C′, and D′). A transformation involves a structural change to an inequivalent state ($R_i \neq R_f$), which may as well include a change in the direction of the symmetry plane. In that case, they are also indicated by *primed* final states.

TABLE II. Forward ($E_{\rm fwd}$) and backward ($E_{\rm bak}$) transition barriers between symmetry equivalent (type R - rotation) and inequivalent (type T - transformation) states of the V_C defect in 4H-SiC. The sublattice site and charge state are shown on the first column. E_i and E_f are initial and final energies, respectively. In type-R mechanisms, the final state $V_C^q(s,R_f)$ has higher energy than the initial state $V_C^q(s,R_i)$. Primed R_f structures indicate a change in the orientation of the mirror plane. All data are in eV.

(s,q)	Type	R_i	R_f	$E_{\rm fwd}$	$E_{\rm bak}$	$E_f - E_i$
$(k,+)$	R	B	B′	0.05		
$(k,+)$	T	B	A	0.12	0.04	0.08
$(k,0)$	R	B	B′	0.41		
$(k,-)$	R	C	C′	0.15		
$(k,-)$	R	D	D′	0.17		
$(k,-)$	T	D	C	0.14	0.12	0.02
$(k,-)$	T	D	C′	0.06	0.04	0.02
$(k,=)$	R	D	D′	0.28		
$(h,+)$	R	B	B′	0.02		
$(h,+)$	T	A	B	0.02	0.02	<0.01
$(h,0)$	R	B	B′	0.30		
$(h,-)$	R	C	C′	0.08		
$(h,-)$	R	D	D′	0.05		
$(h,-)$	T	C	D	0.24	0.10	0.14
$(h,-)$	T	C	D′	0.17	0.03	0.14
$(h,=)$	R	D	D′	0.25		

For $V_C^+(k)$, we have two low-energy structures, namely, A (metastable) and B (ground state). The simple B $\leftrightarrow$ B′ rotation mechanism involves surmounting a small 0.05 eV barrier. On the other hand, the B $\rightarrow$ A transformation has a 0.12 eV barrier, and so it has the alternative B $\rightarrow$ A $\rightarrow$ B′ combined rotation mechanism. For $V_C^+(h)$, structure A was found to be more stable than B by less than 1 meV, so we consider them essentially degenerate. Both rotation of the mirror plane in B $\leftrightarrow$ B′ as well as the A $\rightarrow$ B transformation involve overcoming a minute barrier of 0.02 eV. Hence, for the k site, the rotation between (symmetric) equivalent B structures should be the first dynamic effect to take place as the temperature is raised from 5 K. On the other hand, for the h site, it appears that even at very low temperatures, $V_C^+(h,A)$ defects may cohabit with $V_C^+(h,B)$ states, with the later being able to hop between different alignments.

$V_C^-(k)$ was found to have low energy in structures C (metastable) and D (ground state), which are separated by only 0.02 eV. Simple rotation mechanisms D $\leftrightarrow$ D′ and C $\leftrightarrow$ C′ involve barriers of 0.17 and 0.15 eV, respectively. The in-plane D $\rightarrow$ C transformation also has a comparable barrier of 0.14 eV. On the other hand, the off-plane transformation D $\rightarrow$ C′ is the most favorable mechanism with a barrier of 0.06 eV. These results suggest that the lowest-temperature dynamic mechanism involving atomic motion in $V_C^-(k)$ should involve a D $\rightarrow$ C′ $\rightarrow$ D″ $\rightarrow \cdots$ sequential transformation. For the h site, the negatively charged vacancy is also stable for structures C and D, although D is now metastable by 0.14 eV. For this reason, in-plane C $\rightarrow$ D and off-plane C $\rightarrow$ D′ transformations involve relatively high barriers of 0.24 and 0.17 eV, respectively, whereas simple rotation mechanisms C $\leftrightarrow$ C′ and D $\leftrightarrow$ D′ have only to overcome 0.08-eV and 0.05-eV barriers. This suggests that at low temperatures, the first thermally activated dynamic effect will involve a simple C $\leftrightarrow$ C′ rotations.

We note that several of the above figures, like $V_C^-(k,D) \rightarrow V_C^-(k,C')$ or $V_C^-(h,D) \rightarrow V_C^-(h,D')$ barriers are rather small. They are close to the error bar of the current methodology and should be considered with caution. However, their relative magnitudes are in line with the lowest-temperature dynamic processes observed in the EPR main signals and hyperfines. Accordingly, raising the temperature above 50 K, the pattern of the $V_C^+(k)$ main line is converted from monoclinic to trigonal. This is assigned to a B $\leftrightarrow$ B′ rotation with a calculated 0.05 eV barrier (estimated experimentally as 14 meV). Above 10 K, the main EPR signal of $V_C^+(h)$ and related HFs suffer a progressive change. Such low temperature is consistent with the minute (0.02 eV) A $\rightarrow$ B transformation barrier. Raising the temperature above 40 K, the $V_C^-(k)$ signal shows a series of different transformations, which can be explained by a sequence D $\rightarrow$ C′ $\rightarrow$ D″ $\cdots$ of transformations with a 0.06 eV barrier. Finally, for $V_C^-(h)$, the measurements indicate that the first thermally activated process is limited by an estimated barrier of 20 meV at about 60–70 K, also in line with our calculated barrier of 0.08 eV for the C $\leftrightarrow$ C′ realignment.

The neutral charge states (both at k and h sites) only have one stable structure and only B $\leftrightarrow$ B′ rotations are possible. For these mechanisms we found relatively high barriers of about 0.4 and 0.3 eV for $V_C^0(k)$ and $V_C^0(h)$, respectively. For double negatively charged defects we also found relatively static defects. Here the ground state is the D structure for $V_C^=(k)$ and $V_C^=(h)$, with respective metastable C structures at 0.26 and 0.22 eV above D. Their respective D $\leftrightarrow$ D′ rotation mechanism were found to be limited by 0.28-eV and 0.25-eV-high barriers.

D. Electrical levels and metastability

The formation energy of V_C defects was calculated using Eq. (3). The results are depicted in Fig. 7, where each diagram includes formation energies under C-rich, stoichiometric and C-poor growth-conditions. In agreement with Ref. [35], the formation energy of neutral $V_C^0(k)$ and $V_C^0(h)$ defects in C-rich material is 4.93 and 5.06 eV, respectively, whereas in C-poor 4H-SiC, these quantities are off-set by $\Delta H_{\rm SiC}^f = -0.62$ to 4.31 and 4.44 eV, respectively. For stoichiometric conditions, E_f values are mid-way between C-rich and C-poor figures. The C-rich results agree very well with the formation enthalpy of 4.8-5.0 eV measured from samples grown under analogous conditions [15,65].

Also like in Ref. [35], we only find negative-U behavior ($U = -0.03$ eV) for the acceptor levels of $V_C(k)$, i.e., we find a $E(=/0) = E_c - 0.63$ eV occupancy level, with $V_C^-(k)$ being metastable irrespectively of the position of the Fermi energy. The acceptors of $V_C(h)$ are located close to $E_c - 0.6$ eV and separated by a rather small but positive $U = 0.03$ eV. Donor levels are estimated between $E_c - 1.56$ eV and $E_c - 1.73$ eV, with $E(0/+)$ and $E(+/++)$ levels being separated by positive $U = 0.07$ eV and 0.17 eV for $V_C(k)$ and $V_C(h)$ defects, respectively.

We may conclude that both acceptor and donor levels are very close to the DLTS measurements of $Z_{1/2}$ at $E_c -$ 0.5-0.7 eV and $EH_{6/7}$ at about $E_c - 1.4$–1.5 eV, respectively,

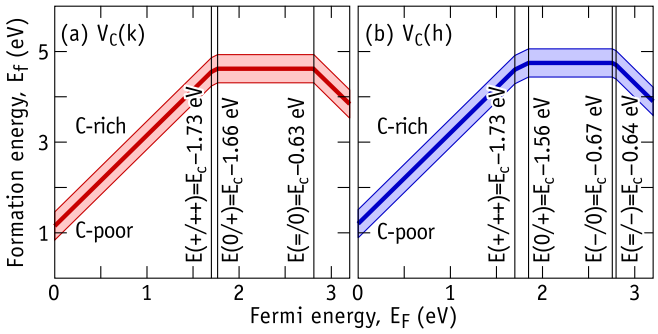

FIG. 7. Formation energy (E_f) of the carbon vacancy at the cubic (a) and hexagonal (b) sites as a function of the Fermi energy (E_F). Lower, central and upper lines represent E_f values for crystals grown under C-poor (or Si-rich), stoichiometric and C-rich conditions.

supporting the assignment of both signals to the carbon vacancy. The relative magnitude of the calculated U values can be connected with the amount of excitation, namely the illumination frequency/intensity and sample temperature needed for the observation of the paramagnetic states. Accordingly, $V_C^-(k)$ is predicted to have $U < 0$ eV and its EPR signal could only be seen in highly doped n-type material under illumination [10], traces of the $V_C^-(h)$ signal, with calculated $U \approx 0$ eV, were detected in darkness at $T > 90$ K [10], both EPR signals of V_C^+, with calculated $U > 0$ eV, could be detected in darkness even at temperatures as low as $T = 5$ K [23]. This trend agrees with our calculated ordering of U values, so that paramagnetic states with smaller (and negative) U values have lower probability to occur because of concurrent formation of energetically favorable diamagnetic states.

While singly negative charge states need some sort of excitation (optical or thermal) to be observed, which is consistent with a negative-U behavior, the EPR data for positively charged vacancies seems actually characteristic of a positive-U ordering of levels. Otherwise, how could we explain the observation of both $V_C^+(k)$ and $V_C^+(h)$ at $T = 5$ K without illumination [23]? To investigate this issue we need to have a more detailed view of the electronic/atomic transitions that take place during DLTS measurements. Combining the relative energies of $V_C^q(s,R)$ states with the calculated rotation/transformation barriers and levels, we arrived at the configuration coordinate diagram of Fig. 8, which describes several electronic emission processes that take place during electrical measurements in n-type material.

Figure 8(a) represents electron emission energies from negative charge states in highly doped n-type material. Here, the Fermi level is located above the acceptor levels. Figure 8(b) represents electron emission energies from donor states in lightly doped n-type material. The Fermi level is now between donor and acceptor levels. Energies on each inset [(a) and (b)] refer to different scales, and the curvature of the potential curves is arbitrary.

We start by analyzing electron emissions in highly doped material from double negatively charge vacancies on the k site. In a DLTS measurement, under a zero-bias filling pulse, all $V_C(k)$ electron traps will be filled with electrons and vacancies will be found in the $V_C^=(k,D)$ state. Around room temperature under reverse bias [6], after a first electron emission with binding energy calculated as 0.64 eV, a second emission with lower energy (0.61 eV) will follow immediately, and the defect will end up in the neutral charge state. The reason for the negative-U behavior of the $V_C(k)$ acceptor sequence is the strong relaxation to structure B after the second emission.

On the hexagonal site, the electron binding energy of $V_C^=(h)$ is 0.64 eV considering a transition between ground states, $V_C^=(h,D) \rightarrow V_C^-(h,C) + e^-$. The second emission from $V_C^-(h,C)$ has a slightly larger binding energy of 0.67 eV, corresponding to a small but positive-U previously shown in Fig. 7(b). This discrepancy with the DLTS data could indicate that the stability of $V_C^-(h,C)$ is overestimated, or alternatively, the stability of $V_C^0(h,B)$ is underestimated.

It is possible that the conversion between C and D configurations could play a role during electron emission. For instance, the calculated energy barrier between $V_C^-(k,D)$ and $V_C^-(k,C)$ is 0.06 eV, which should be compared with 0.02 eV from analysis of the thermally activated motional effects

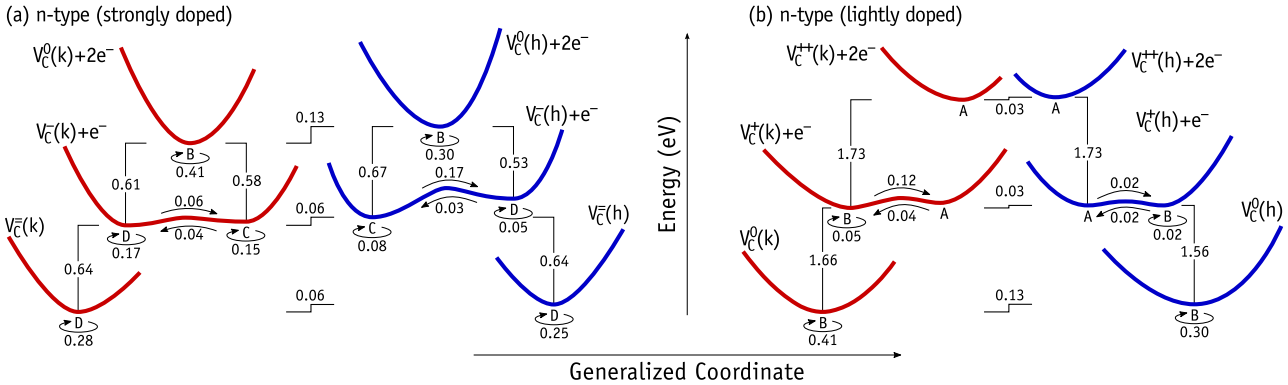

FIG. 8. Configuration coordinate diagram of V_C defects in 4H-SiC. Acceptor and donor transitions are shown in (a) and (b), representing strongly doped and lightly doped n-type material, respectively. Electronic transitions (up in energy) involve the emission of one electron to the conduction band (e^-). Insets (a) and (b) include two diagrams, one for each sublattice site. Energies (in eV) are accompanied with guidelines for better perception. Forward/backward transformation and rotation barrier energies are indicated by right/left and spinning arrows, respectively. Steplike guidelines indicate the energy difference between ground states of defects in k and h sites. Minima of the potential curves represent stable/metastable structures and are identified with labels A–D.

observed in EPR [29]. Since atomic rotations/transformations occur on a much faster time-scale than electronic transitions, we cannot exclude the possibility that at the temperature of the DLTS measurements, emission from V_C^- could initiate from metastable states, thus leading to an effective smaller second ionization.

In as-grown material, where vacancies are in equilibrium conditions, Ref. [6] reports a $Z_2(-/0)$ peak which was about twice the intensity of $Z_1(-/0)$. This contrasts with irradiated material where $Z_1(-/0)$ and $Z_2(-/0)$ show up with about the same magnitude. Since carbon vacancies are invariably more stable in the cubic site (by about 0.06 eV in n-type SiC as shown in Fig. 8), we attribute Z_2 and Z_1 signals to $V_C(k)$ and $V_C(h)$, respectively. A 1:2 intensity ratio corresponds to a concentration ratio $[V_C(h)] : [V_C(k)] = \exp(-0.06/k_BT)$ under equilibrium conditions at $T \approx 1000$ K. This assignment is also consistent with a previous connection between Z_1 and $V_C(h)$ by photo-EPR [10], it is supported by the lower calculated U-value for the acceptor levels of $V_C(k)$ [when compared to $V_C(h)$], and it agrees with the calculated deeper $(-/0)$ transition for $V_C(h)$ than $V_C(k)$. We finally note that the calculated $U = +0.03$ eV between $(-/0)$ and $(=/-)$ acceptors of $V_C(h)$ must not be far from the true value. This value is consistent with the observation of the $V_C^-(h)$ EPR signal at 100 K (without illumination) and its photoionization with photon energies $h\nu > 0.74$ eV below the band-gap threshold [10]. In contrast, the analogous photoionization for the cubic vacancy could not be observed, most probably because U is more negative and the most favorable $V_C(k)$ defects are diamagnetic.

The calculated donor levels are also represented in Fig. 8(b). Although first and second electron binding energies, i.e., $(0/+)$ and $(+/++)$ transitions, are close for both sublattice sites, they do not form a negative-U sequence. The U-value for $V_C(k)$ is $1.73 - 1.66 = 0.07$ eV, while for the h-site $U = 0.17$ eV. These results are in partial agreement with the data reported by Booker *et al.* [17], where $U = -0.04$ eV for EH7 and $U = 0.03 \pm 0.04$ eV for EH6, obviously favoring the assignment of $V_C(k)$ and $V_C(h)$ to EH7 and EH6, respectively. Again, we may use the relative stability of $V_C(k)$ and $V_C(h)$ to identify the sublattice sites of EH7 and EH6 signals. In as-grown material and electron irradiated samples subject to high-temperature anneals, the EH6:EH7 ratio was found to be about 4:5 [16], suggesting that EH7 is more stable. The relative energies in Figure 8(b), confirm that EH_6 and EH_7 should therefore be connected to$V_C(h)$ and $V_C(k)$, respectively.

Of course, there is some degree of uncertainty in the calculated magnitudes (and sign) of the U values. Within the present level of theory, electronic levels are usually affected by error bars of about ∼0.1 eV due to spurious (strain, Coulomb, or dispersive) periodic interactions. However, as we will point out in the next section, there is further experimental evidence for a positive-U ordering of donor transitions.

IV. DISCUSSION

We start by addressing the strong temperature dependence of the EPR data related to $V_C^+(h)$. The $V_C^+(h)$ defect in 4H-SiC has the properties of a pJT distorted structure in the weak-coupling regime, where the pseudo-Jahn-Teller relaxation energy is much smaller than the Debye frequency, $E_{pJT} \ll \hbar\omega_D$ [58]. For the case of 4H-SiC we have $\hbar\omega_D = 103$ meV [66]. We note that the vibronic softening constant, as it is described in Eq. (12), only accounts for a single distortion mode. However, for an accurate account of the pJT vibronic details of a defect in a crystal, a continuum of fundamental and excited vibrational modes would have to be included in the summation. Since this is not practical, we leave a qualitative description supported on the agreement between adiabatic calculations and the measurements. Hence, for temperatures approaching 0 K, all zero-phonon vibrations obeying the selection rules will contribute to the vibronic force constant k_v^R. If this contribution is not strong enough to produce a negative curvature of the APES at $R = A$, the vacancy will preserve the $|a_1^1\rangle \sim |3\bar{1}\bar{1}\bar{1}\rangle$ state. This could be the case for $V_C^+(h)$ since there is good agreement between the magnitude of the low-T hyperfines shouldering the EI6 EPR signal and those calculated for $V_C^+(h,A)$ [22,23]. For instance, at $T = 10$ K the Si_1 HF components parallel and perpendicular to the crystallographic c-axis were measured as $A_\parallel = 434$ MHz and and $A_\perp = 297$ MHz, respectively [27]. These are to be compared with $A_\parallel = 400$ MHz and and $A_\perp = 275$ MHz calculated for $V_C^+(h,A)$ [22]. With increasing temperature, additional phonon modes are populated, and k_v^R becomes more negative. Should $k_v^R < -k_0^R$, the $V_C^+(h,B)$ state $|a_-'^1\rangle$ will be lower in energy and the observed HFs should be converted to those of the monoclinic defect. The calculations from Ref. [22] anticipate that this transformation would lead to a Si_1 HF splitting with $A_\parallel = 313$ MHz and $A_\perp = 215$ MHz, which would explain the strong and progressive decrease of the observed HF data to $A_\parallel = 344$ MHz and $A_\perp = 237$ MHz at $T = 293$ K [27].

The observed trigonal pattern for the EI6 main signal and related hyperfines between 5 K and room temperature can also be explained based on dynamic arguments. Around $T = 5$-10 K, the HF signals arise from the $|a_1^1\rangle \sim |3\bar{1}\bar{1}\bar{1}\rangle$ state. This static trigonal state accounts for the observed ∼40% localization of the paramagnetic wave function on Si_1 [27]. On the other hand, at higher temperatures, the distorted $|a_-'^1\rangle$ state is expected to quickly hop between all three equivalent states $|11\bar{1}\bar{1}\rangle$, $|1\bar{1}1\bar{1}\rangle$, and $|\bar{1}11\bar{1}\rangle$. Our calculated hopping barrier of 0.02 eV is compatible with this behavior. Since the three states lead to approximately the same spin-density amplitude and shape on all four Si radicals, the result is the observation of two trigonal HF signals. One of them corresponds to Si_1, while the other represents a shell of the three $Si_{2\text{-}4}$ atoms, also explaining the observed 1:3 amplitude ratio [27].

The complex temperature dependence of the $V_C^-(k)$ EPR signal and related hyperfine peaks can also be discussed with help of dynamic arguments. Below $T \approx 40$ K, the EPR data shows a C_{1h} symmetric defect with one pair of HF shoulders due to mirror-symmetric $Si_{3,4}$ radicals. This is consistent with the static D structure with paramagnetic ground state $|a_-'^2\, a''^1\, a_+'\rangle \sim |00\bar{1}1\rangle$ [30]. Increasing the temperature above 40 K leads to the quenching of the $Si_{3,4}$ HF signal and the angular dependence of the main signal acquires a trigonal shape. Based on the energy difference between $V_C^-(k,D)$ and $V_C^-(k,C)$ (0.02 eV), as well as on the calculated rotation and transformation barriers from Table II and Fig. 8, we suggest that this effect is connected to the off-plane $D \rightarrow C' \rightarrow D''$

transformation, which is limited by a barrier estimated as $E_{\rm fwd} = 0.06$ eV. Such a sequence effectively leads to the alternation between structures C and D and to the rotation of the mirror plane of the defect. This mechanism translates into alternate transitions between symmetry-equivalent $|00\bar{1}1\rangle$ and $|\bar{1}100\rangle$ conjugate states from structures D and C, respectively. The amplitude of the spin-density on the basal radicals becomes *intermittent*, explaining the disappearance of these HFs from the $V_C^-(k,D)$ spectrum at $T \approx 40$ K. Above $T \approx$ 40–80 K, new trigonal Si_1 and $Si_{2\text{-}4}$ HFs appear in the EPR spectrum, which are assigned to the combined thermally activated population and rotation of both $V_C^-(k,D)$ and $V_C^-(k,C)$ states [30]. However, this argument is incompatible with the above referred localization intermittency which is expected to work above 80 K as well. We note that unlike in $|a''^1\rangle$ of $V_C^-(k,D)$, the symmetry of the $|a'^1_+\rangle \sim |1\bar{1}00\rangle$ state of $V_C^-(k,C)$ does not impose zero amplitude of the wave function at any of the Si nuclei. The spin-density on Si_3 and Si_4 is actually small but not zero (see Fig. 4). We suggest that for $T >$ 40-80 K the $V_C^-(k,D)$ HFs are quenched due to intermittency effects, while $V_C^-(k,C)$ becomes populated and its HF-related features increase in the spectrum. During the thermally activated motion of $V_C^-(k,C)$, the Si nuclei in the basal plane always contribute with a nonzero hyperfine interaction. This could explain the appearance of the weak and broad $Si_{2\text{-}4}$ trigonal HF at about 80 K. $V_C^-(k,C)$ with $|a'^2_- a'^1_+ a''\rangle$ filling order is expected to show a temperature-dependent pJT effect due increasing coupling between a' states. This would lead to the stabilization of this state, making it consistent with the strong temperature dependence of the Si_1 HF axial component, which increases from 28 MHz at 60 K to 103 MHz at 140 K [30].

An identical argument can applied to $V_C^-(h)$, which adopts the ground state structure C. In this case, structure D is metastable by 0.14 eV, the lowest C $\rightarrow$ D transformation barrier is 0.17 eV and $V_C^-(h,D)$ does not appear in the spectrum. Below $T \approx 60$ K, the $V_C^-(h,C)$ state is static ($|a'^1_+\rangle \sim |1\bar{1}00\rangle$) with two inequivalent HFs on Si_1 and Si_2 on the symmetry plane. Above ~70K, the available thermal energy promotes the C $\leftrightarrow$ C′ rotation mechanism (with calculated barrier of 0.08 eV), and the spin-density intermittency on $Si_{2\text{-}4}$ nuclei results in the observation of a single Si_1 axial HF. This was explained in Ref. [30]. Increasing further the temperature above 120 K, led to the appearance of a trigonal $Si_{2\text{-}4}$ HF signal, which is in conflict with the intermittency argument. Again, we suggest that raising the temperature also increases the magnitude of the vibronic term for structure C, and that increases the amplitude of the $|a'^1_+\rangle \sim |1\bar{1}00\rangle$ wave function on Si_3 and Si_4 by further increasing the $|e'\rangle$ contribution to $|a'_+\rangle$. The result is a dynamic state with amplitude on all Si radicals, and a reconciliation of the model with the observations.

The reason for $V_C^-(k)$ showing a nodal (a'') ground state, as opposed to $V_C^-(h)$, which is a symmetric ground state (a'), is also due to the weaker crystal-field on site k. As depicted in Fig. 3, for $V_C^-(k)$ the Coulomb interaction between $|a'_-\rangle$ and $|a'_+\rangle$ states causes a crossing of levels between the neutral and the single negatively charged states, and that results in a more stable $|a'^2_- a''^1 a'_+\rangle$ filling order. Also in Fig. 3, it is evident that the stabilization of the $|a'^2_- a'^1_+ a''\rangle$ filling on the h site indicates that the repulsion between symmetric states is weaker. Hence the crossing effect observed in $V_C^-(k)$, is now obtained for the double negative charge state in $V_C^=(h)$.

Finally, we would like to underline a fundamental issue regarding the assignment of $EH_{6/7}$ to the superposition of negative-U double donors from $V_C(k)$ and $V_C(h)$ [17]. If that was indeed the case, the peak amplitude of $EH_{6/7}$ would have to match that of $Z_{1/2}$, and that is usually not observed by DLTS. In fact, it is widely documented that $EH_{6/7}$ has a smaller amplitude than $Z_{1/2}$, irrespective of the sample history, including as-grown, irradiated/implanted plus annealing and thermal processed (see, for example, Refs. [15,16,21,67]). This led the authors from Ref. [15] to the suggestion that $EH_{6/7}$ is a single donor transition. Our calculations are consistent with a broad $EH_{6/7}$ signal made of closely spaced positive-U ordered double donor levels of the vacancy in different sublattice sites. Further support for the positive-U sequence of donor levels come from the relative formation energies of V_C for different charge states. From these figures we can estimate the fraction of positively charged vacancies, f_+ (with respect to total amount of V_C defects) when the Fermi level is located halfway between the (0/+) and (+/ ++) levels,

$$f_+ = \frac{\exp(U/2k_BT)}{2 + \exp(U/2k_BT)}, \tag{16}$$

which for a negative-U center means that the Fermi level is locked at the (0/ ++) transition. Equation (16) neglects the formation of negatively charged vacancies, it assumes that V_C^0, V_C^+, and V_C^{++} states are in thermal equilibrium at temperature T, and k_B is the Boltzmann constant. Hence, at $T = 5$ K and considering $U = -0.04$ eV reported for EH_7 by Booker *et al.* [17], we arrive at $f_+ \sim 10^{-21}$, essentially telling us that under these conditions all vacancies would be EPR-inactive. This strongly indicates that the real U value of EH_7 defect should be positive. Analogous conclusions would be drawn for EH_6.

V. CONCLUSIONS

We report on density functional calculations of the electronic and dynamic properties of the carbon vacancy in 4H-SiC using semilocal and hybrid functionals. The defect exhibits a rich catalog of structures that depend on the sublattice site and charge state. Their occurrence is rationalized on the basis of several effects, namely the character of the occupied one-electron states, the site-dependence of the crystal-field, and the magnitude of the pseudo-Jahn-Teller effect. Diamagnetic states show either strong or no pseudo-Jahn-Teller effect and possess a relatively deep potential energy surface. They display stable ground state structures A, B, and D for charge states $q = +2, 0$, and -2, respectively, no matter their sublattice site. Conversely, paramagnetic charge states $q = +1$ and $q = -1$ suffer from weak pseudo-Jahn-Teller distortions. Here, ground states are, respectively, B and D for the k site, whereas they are respectively A and C for the h site. This structural variety essentially arises from the stronger crystal field on the h site that stabilizes electronic states polarized along the main axis. Also for the paramagnetic states, and depending on the strength of the vibronic coupling within the pseudo-Jahn-Teller effect, metastable structures play an important role in the behavior of the vacancy as a function of temperature. For charge states

$q = +1$ and $q = -1$, structures A and C are metastable in the sublattice site k, respectively, while structures B and D are metastable in the sublattice site h.

Mechanisms for the transformation between these structures, as well as for the rotation of the mirror plane for monoclinic structures (B, C, and D) were calculated and discussed in the light of the temperature-dependence of the EPR data. From the total energies, electrical levels and nudged elastic band calculations we constructed a configuration coordinate diagram which considers electronic transitions, as well as structure rotations and transformations between the relevant configurations.

Regarding the electrical activity, our results support the assignment of $Z_{1/2}$ and $EH_{6/7}$ DLTS signals to the acceptor and donor transitions of the carbon vacancy. We were able to attribute a sublattice site to each component of the DLTS signals based on (i) the correlation between the relative magnitudes of the calculated and measured U-values, and (ii) the correlation between the site-dependent formation energies and the relative intensity of the DLTS peaks in as-grown material. Accordingly, we support the assignment of Z_1 and Z_2 DLTS peaks to $(=/0)$ two-electron cascade emissions from $V_C^{=}(h)$ and $V_C^{=}(k)$ defects, respectively. We were able to apply analogous arguments to the donor transitions. In this case, we assign EH_6 and EH_7 peaks to electron emissions from $V_C(h)$ and $V_C(k)$ defects, respectively. Our results favor a positive-U ordering for the donor transitions in both sublattice sites. Hence each peak should result from $(0/+)$ and $(+/++)$ transitions with very close emissions rates. Although this is at variance with recent electrical measurements [17], they are consistent with the low-temperature EPR data acquired in darkness.

ACKNOWLEDGMENTS

We would like to thank Prof. Bengt Svensson for providing fruitful comments and criticisms. This work was jointly supported by the Science for Peace and Security NATO Program through project SPS 985215, and by the *Fundação para a Ciência e a Tecnologia* (FCT) through project UID/CTM/50025/2013. The authors would like to further acknowledge the computer resources provided by the Swedish National Infrastructure for Computing (SNIC) at PDC.

[1] *SiC Materials and Devices*, edited by Y. S. Park, 1st ed., Semiconductors and Semimetals (Academic Press, San Diego, 1998), Vol. 52.
[2] *Fundamentals of Silicon Carbide Technology*, edited by T. Kimoto and J. A. Cooper (Wiley, Singapore, 2014).
[3] N. Iwamoto and B. G. Svensson, *Defects in Semiconductors* (Elsevier, Waltham, MA 02451, 2015), Chap. 10, pp. 369–407.
[4] R. Nipoti, U. Grossner, and G. Alfieri, in *Silicon Carbide and Related Materials 2014*, Materials Science Forum Vol. 821 (Trans Tech Publications, Switzerland, 2015), pp. 381–386.
[5] T. Kimoto, A. Itoh, H. Matsunami, S. Sridhara, L. L. Clemen, R. P. Devaty, W. J. Choyke, T. Dalibor, C. Peppermüller, and G. Pensl, Appl. Phys. Lett. **67**, 2833 (1995).
[6] C. Hemmingsson, N. T. Son, O. Kordina, J. P. Bergman, E. Janzén, J. L. Lindström, S. Savage, and N. Nordell, J. Appl. Phys. **81**, 6155 (1997).
[7] T. Hiyoshi and T. Kimoto, Appl. Phys. Express **2**, 041101 (2009).
[8] C. G. Hemmingsson, N. T. Son, A. Ellison, J. Zhang, and E. Janzén, Phys. Rev. B **58**, R10119 (1998).
[9] C. G. Hemmingsson, N. T. Son, A. Ellison, J. Zhang, and E. Janzén, Phys. Rev. B **59**, 7768 (1999).
[10] N. T. Son, X. T. Trinh, L. S. Løvlie, B. G. Svensson, K. Kawahara, J. Suda, T. Kimoto, T. Umeda, J. Isoya, T. Makino, T. Ohshima, and E. Janzén, Phys. Rev. Lett. **109**, 187603 (2012).
[11] G. D. Watkins, in Negative-U properties for defects in solids, in *Advances in Solid State Physics*, edited by P. Grosse (Springer Berlin Heidelberg, Berlin, Heidelberg, 1984), pp. 163–189.
[12] K. Dmowski, Rev. Sci. Instrum. **61**, 1319 (1990).
[13] M. O. Aboelfotoh and J. P. Doyle, Phys. Rev. B **59**, 10823 (1999).
[14] A. Koizumi, V. P. Markevich, N. Iwamoto, S. Sasaki, T. Ohshima, K. Kojima, T. Kimoto, K. Uchida, S. Nozaki, B. Hamilton, and A. R. Peaker, Appl. Phys. Lett. **102**, 032104 (2013).
[15] H. M. Ayedh, V. Bobal, R. Nipoti, A. Hallén, and B. G. Svensson, J. Appl. Phys. **115**, 012005 (2014).
[16] K. Danno and T. Kimoto, Jpn. J. Appl. Phys. **45**, L285 (2006).
[17] I. D. Booker, E. Janzén, N. T. Son, J. Hassan, P. Stenberg, and E. Ö. Sveinbjörnsson, J. Appl. Phys. **119**, 235703 (2016).
[18] L. Storasta, J. P. Bergman, E. Janzén, A. Henry, and J. Lu, J. Appl. Phys. **96**, 4909 (2004).
[19] S. A. Reshanov, G. Pensl, K. Danno, T. Kimoto, S. Hishiki, T. Ohshima, H. Itoh, F. Yan, R. P. Devaty, and W. J. Choyke, J. Appl. Phys. **102**, 113702 (2007).
[20] B. Zippelius, A. Glas, H. B. Weber, G. Pensl, T. Kimoto, M. Krieger, Mater. Sci. Forum **717-720**, 251 (2011).
[21] G. Alfieri and T. Kimoto, Appl. Phys. Lett. **102**, 152108 (2013).
[22] M. Bockstedte, M. Heid, and O. Pankratov, Phys. Rev. B **67**, 193102 (2003).
[23] T. Umeda, J. Isoya, N. Morishita, T. Ohshima, T. Kamiya, A. Gali, P. Deák, N. T. Son, and E. Janzén, Phys. Rev. B **70**, 235212 (2004).
[24] N. T. Son, P. N. Hai, and E. Janzén, Phys. Rev. B **63**, 201201 (2001).
[25] M. E. Zvanut and V. V. Konovalov, Appl. Phys. Lett. **80**, 410 (2002).
[26] V. V. Konovalov, M. E. Zvanut, and J. van Tol, Phys. Rev. B **68**, 012102 (2003).
[27] T. Umeda, J. Isoya, N. Morishita, T. Ohshima, and T. Kamiya, Phys. Rev. B **69**, 121201 (2004).
[28] V. Y. Bratus', T. T. Petrenko, S. M. Okulov, and T. L. Petrenko, Phys. Rev. B **71**, 125202 (2005).
[29] T. Umeda, Y. Ishitsuka, J. Isoya, N. T. Son, E. Janzén, N. Morishita, T. Ohshima, H. Itoh, and A. Gali, Phys. Rev. B **71**, 193202 (2005).

[30] X. T. Trinh, K. Szász, T. Hornos, K. Kawahara, J. Suda, T. Kimoto, A. Gali, E. Janzén, and N. T. Son, Phys. Rev. B **88**, 235209 (2013).
[31] A. Zywietz, J. Furthmüller, and F. Bechstedt, Phys. Rev. B **59**, 15166 (1999).
[32] K. Kawahara, X. T. Trinh, N. T. Son, E. Janzén, J. Suda, and T. Kimoto, Appl. Phys. Lett. **102**, 112106 (2013).
[33] K. Kawahara, X. T. Trinh, N. T. Son, E. Janzén, J. Suda, and T. Kimoto, J. Appl. Phys. **115**, 143705 (2014).
[34] M. Bockstedte, A. Marini, O. Pankratov, and A. Rubio, Phys. Rev. Lett. **105**, 026401 (2010).
[35] T. Hornos, A. Gali, B. G. Svensson, Mater. Sci. Forum **679-680**, 261 (2011).
[36] G. Kresse and J. Hafner, Phys. Rev. B **47**, 558 (1993).
[37] G. Kresse and J. Hafner, Phys. Rev. B **49**, 14251 (1994).
[38] G. Kresse and J. Furthmüller, Comput. Mater. Sci. **6**, 15 (1996).
[39] G. Kresse and J. Furthmüller, Phys. Rev. B **54**, 11169 (1996).
[40] P. E. Blöchl, Phys. Rev. B **50**, 17953 (1994).
[41] J. Heyd, G. E. Scuseria, and M. Ernzerhof, J. Chem. Phys. **118**, 8207 (2003).
[42] A. V. Krukau, O. A. Vydrov, A. F. Izmaylov, and G. E. Scuseria, J. Chem. Phys. **125**, 224106 (2006).
[43] J. P. Perdew, K. Burke, and M. Ernzerhof, Phys. Rev. Lett. **77**, 3865 (1996).
[44] P. Grivickas, V. Grivickas, J. Linnros, and A. Galeckas, J. Appl. Phys. **101**, 123521 (2007).
[45] Z. Li and R. C. Bradt, J. Appl. Phys. **60**, 612 (1986).
[46] G. Makov and M. C. Payne, Phys. Rev. B **51**, 4014 (1995).
[47] H.-P. Komsa, T. T. Rantala, and A. Pasquarello, Phys. Rev. B **86**, 045112 (2012).
[48] C. Freysoldt, J. Neugebauer, and C. G. Van de Walle, Phys. Rev. Lett. **102**, 016402 (2009).
[49] Y. Kumagai and F. Oba, Phys. Rev. B **89**, 195205 (2014).
[50] S. Baroni and R. Resta, Phys. Rev. B **33**, 7017 (1986).
[51] E. Cockayne and B. P. Burton, Phys. Rev. B **62**, 3735 (2000).
[52] L. Patrick and W. J. Choyke, Phys. Rev. B **2**, 2255 (1970).
[53] C. W. M. Castleton, A. Höglund, and S. Mirbt, Phys. Rev. B **73**, 035215 (2006).
[54] G.-X. Qian, R. M. Martin, and D. J. Chadi, Phys. Rev. B **38**, 7649 (1988).
[55] L. Hedin and S. Lundqvist, Solid State Phys. **23**, 1 (1970).
[56] E. Greenberg, C. A. Natke, and W. N. Hubbard, J. Chem. Thermodyn. **2**, 193 (1970).
[57] G. Henkelman, B. P. Uberuaga, and H. Jónsson, J. Chem. Phys. **113**, 9901 (2000).
[58] I. Bersuker, *The Jahn-Teller Effect* (Cambridge University Press, Cambridge, 2006).
[59] I. B. Bersuker, Chem. Rev. **113**, 1351 (2013).
[60] R. F. W. Bader and A. D. Bandrauk, J. Chem. Phys. **49**, 1666 (1968).
[61] R. G. Pearson, J. Am. Chem. Soc. **91**, 1252 (1969).
[62] R. G. Pearson, Comput. Math. Appl. **12**, 229 (1986).
[63] I. B. Bersuker, N. B. Balabanov, D. Pekker, and J. E. Boggs, J. Chem. Phys. **117**, 10478 (2002).
[64] P. García-Fernández, J. A. Aramburu, M. T. Barriuso, and M. Moreno, Phys. Rev. B **73**, 184122 (2006).
[65] H. M. Ayedh, R. Nipoti, A. Hallén, and B. G. Svensson, Appl. Phys. Lett. **107**, 252102 (2015).
[66] G. A. Slack, J. Appl. Phys. **35**, 3460 (1964).
[67] J. Wong-Leung and B. G. Svensson, Appl. Phys. Lett. **92**, 142105 (2008).